

Measuring, processing, and analyzing hysteresis data

Greig A. Paterson^{1, 2, 3}, Xiang Zhao⁴, Mike Jackson⁵ and David Heslop⁴

¹ Department of Earth, Ocean and Ecological Sciences, University of Liverpool, Liverpool L69 7ZE, UK.

² Key Laboratory of Earth and Planetary Physics, Institute of Geology and Geophysics, Chinese Academy of Sciences, Beijing 100029, China.

³ Institutions of Earth Science, Chinese Academy of Sciences, Beijing 100029, China.

⁴ Research School of Earth Sciences, The Australian National University, Canberra, ACT 2601, Australia.

⁵ Institute for Rock Magnetism, Winchell School of Earth Sciences, University of Minnesota, Minnesota, USA.

12

Corresponding author: Greig A. Paterson (greig.paterson@liverpool.ac.uk)

14

Key Points:

- Magnetic hysteresis loops are one of the most widely used rock magnetic data types in Earth sciences
- We outline a broad range of strategies to measure better data and more accurately analyze results
- We introduce *HystLab*, a new software package that incorporates these methods and the ability to produce publication ready figures

22

23

24 **Abstract**

25 Magnetic hysteresis loops are important in theoretical and applied rock magnetism with
26 applications to paleointensities, paleoenvironmental analysis, and tectonic studies, among many
27 others. Information derived from these data is amongst the most ubiquitous rock magnetic data
28 used by the Earth science community. Despite their prevalence, there are no general guidelines to
29 aid scientists in obtaining the best possible data and no widely available software to allow the
30 efficient analysis of hysteresis loop data using the most advanced and appropriate methods. Here
31 we outline detrimental factors and simple approaches to measuring better hysteresis data and
32 introduce a new software package called *Hysteresis Loop analysis box (HystLab)* for processing
33 and analyzing loop data. Capable of reading a wide range of data formats, *HystLab* provides an
34 easy-to-use interface allowing users to visualize their data and perform advanced processing,
35 including loop centering, drift correction, high-field slope corrections, as well as loop fitting to
36 improve the results from noisy specimens. A large number of hysteresis loop properties and
37 statistics are calculated by *HystLab* and can be exported to text files for further analysis. All plots
38 generated by *HystLab* are customizable and user preferences can be saved for future use. In
39 addition, all plots can be exported to encapsulated postscript files that are publication ready with
40 little or no adjustment. *HystLab* is freely available for download at
41 <https://github.com/greigpaterson/HystLab> and in combination with our simple measurement guide
42 should help the paleo- and rock magnetic communities get the most from their hysteresis data.

43

44

45 **Keywords:** magnetic hysteresis; rock magnetism; paleomagnetism, software

46

47

48 **1 Introduction**

49 The use of magnetic hysteresis data is prevalent throughout paleomagnetic and Earth science
50 studies. It has applications in fundamental rock magnetism (Krása et al., 2009; Williams et al.,

51 2010), analyzing paleointensity data (Haag et al., 1995; Carvallo et al., 2006; Kissel et al., 2011;
52 Paterson et al., 2016; Paterson et al., 2017), paleoclimate and paleoenvironmental studies (Liu et
53 al., 2015; Chang et al., 2016; Zhang et al., 2016; Hatfield et al., 2017), biomagnetism (Pan et al.,
54 2005; Lin and Pan, 2009; Li et al., 2010), tectonics (Van Hinsbergen et al., 2008; Jackson and
55 Swanson-Hysell, 2012; Li et al., 2017), pollution monitoring (Muxworthy et al., 2001; Zhang et al.,
56 2013), and extraterrestrial magnetism (Muxworthy et al., 2017; Tikoo et al., 2017), among many
57 others. Despite this widespread usage, the analysis of hysteresis data can be non-trivial and
58 detrimental effects on the quality and accuracy of hysteresis data, such as off-center loops and
59 drift are routinely unaccounted for (Jackson and Solheid, 2010).

60 Following a brief introduction to magnetic hysteresis, here we present some general guidelines for
61 the improved measurement of magnetic hysteresis data and new graphical user interface software,
62 *Hysteresis Loop analysis box (HystLab)*, for the advanced processing and analysis of hysteresis
63 loops. *HystLab* follows closely the recommendations proposed by von Dobeneck (1996) and in
64 particular those of Jackson and Solheid (2010). In this introduction to *HystLab*, we briefly outline
65 these procedures taking note of differences employed in our new software package.

66 Written in MATLAB, *HystLab* will run on all Windows, OS X, and Linux systems capable of running
67 MATLAB v8 or above (no additional toolboxes are required). The *HystLab* package is available for
68 download from <https://github.com/greigpaterson/HystLab> and installation and operating instructions
69 are given in the provided documentation.

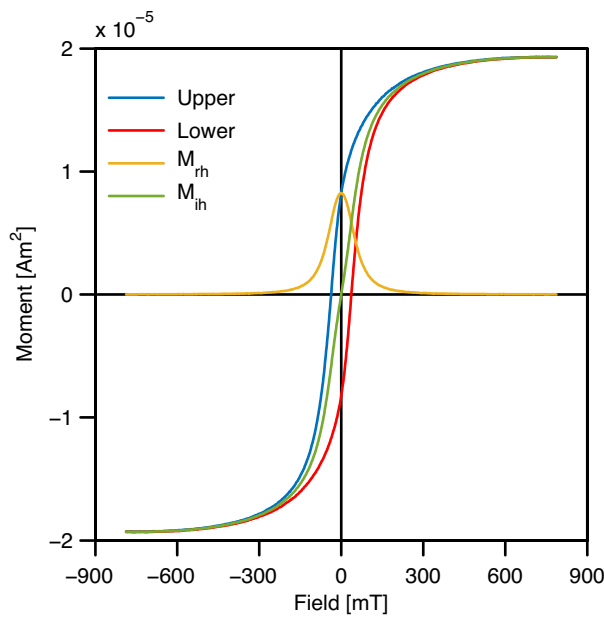
70

71 **2 The basics of magnetic hysteresis**

72 Measurement of a magnetic hysteresis loop begins by firstly saturating the magnetic moment (M)
73 of a specimen in large positive (or negative) field (B). The intensity of the field is decreased to zero
74 and increased in the opposite direction to negative (or positive) saturation (blue branch in Figure
75 1). Finally, the field is swept back to positive (or negative) saturation to complete the loop (red
76 branch in Figure 1). The sweep from positive to negative saturation is termed the upper branch
77 and the sweep from negative to positive saturation is termed the lower branch (Figure 1). Under

78 idealized conditions and for most specimens of natural material, the upper and lower branches are
 79 inverse (rotation) symmetric around the origin. That is, any point (B_i, M_i) on a loop can be inverted
 80 around the origin to $(-B_i, -M_i)$, and lie exactly on the opposite branch. There are, of course, physical
 81 reasons why a hysteresis loop may not be centered and symmetric about the origin (e.g., Housen
 82 et al., 1996; Harrison et al., 2007), but for most geological materials it is reasonable to assume
 83 origin-centered symmetry, and deviations from symmetry can then be attributed to undesirable
 84 factors such as measurement noise, drift, and/or offsets.

85



86

87 **Figure 1. Example hysteresis loop.** A basic hysteresis loop distinguishing the upper and lower
 88 branches as well as the remanent (M_{rh}) and induced (M_{ih}) hysteretic curves.

89

90 Given the inverse symmetry expected for geological materials, when the lower branch of a noise-
 91 free hysteresis loop is inverted about the origin it will lie exactly on the upper branch. In practice,
 92 however, the match is rarely exact and the difference between the upper and inverted lower
 93 branch can be viewed as an estimate of the noise of a hysteresis measurement. This is the $err(H)$
 94 curve of Jackson and Solheid (2010), herein simply called the noise curve.

95 A basic hysteresis loop can be further processed into remanence and induced hysteretic curves
96 (Rivas et al., 1981; von Dobeneck, 1996; Figure 1). The remanence hysteretic curve, M_{rh} , is half
97 the difference between the upper and lower hysteresis branches, while the induced hysteretic
98 curve, M_{ih} , is half the sum of the upper and lower hysteresis branches. Like a basic hysteresis
99 loop, both M_{rh} and M_{ih} have expected symmetries: reflection symmetry about the vertical axis and
100 rotation symmetry about the origin, respectively.

101 **3 Measuring a hysteresis loop**

102 Regardless of the sophistication of data processing and analysis, low quality data will always yield
103 low quality results. In this section, we briefly outline some common artifacts in hysteresis loop data
104 and simple approaches for improving the measurement quality of a hysteresis loop. These
105 guidelines are particularly aimed at Princeton Measurements Corporation MicroMag 3900 vibrating
106 sample magnetometers (VSMs) (now owned by Lake Shore Cryotronics, Inc.) as these are the
107 most widely used instruments in the rock magnetic community and are the ones with which we
108 have most experience. Nevertheless, the basic ideas behind these recommendations are
109 applicable to a wide range of equipment capable of measuring magnetic hysteresis loops.
110 Similarly, many of these recommendations can be used to improve data for other measurements
111 that can be performed on these types of instruments (e.g., isothermal remanent acquisition curves,
112 or first-order reversal curves).

113 **3.1 Improving signal-to-noise**

114 Most VSMs have a number of settings that can be used to improve the signal-noise-ratio of a
115 hysteresis loop. This includes the physical setup of the experiments such as the size of the
116 specimen and the spacing between the sensing/pick-up coils (pole gap), as well as software and
117 measurement protocol settings such as the measurement average time, the field sweep mode,
118 field stabilization time, as well as averaging multiple loops. The trade-off for measuring a higher
119 quality loop, however, is a longer measurement time per specimen, which may result in larger drift
120 during measurement of a single loop.

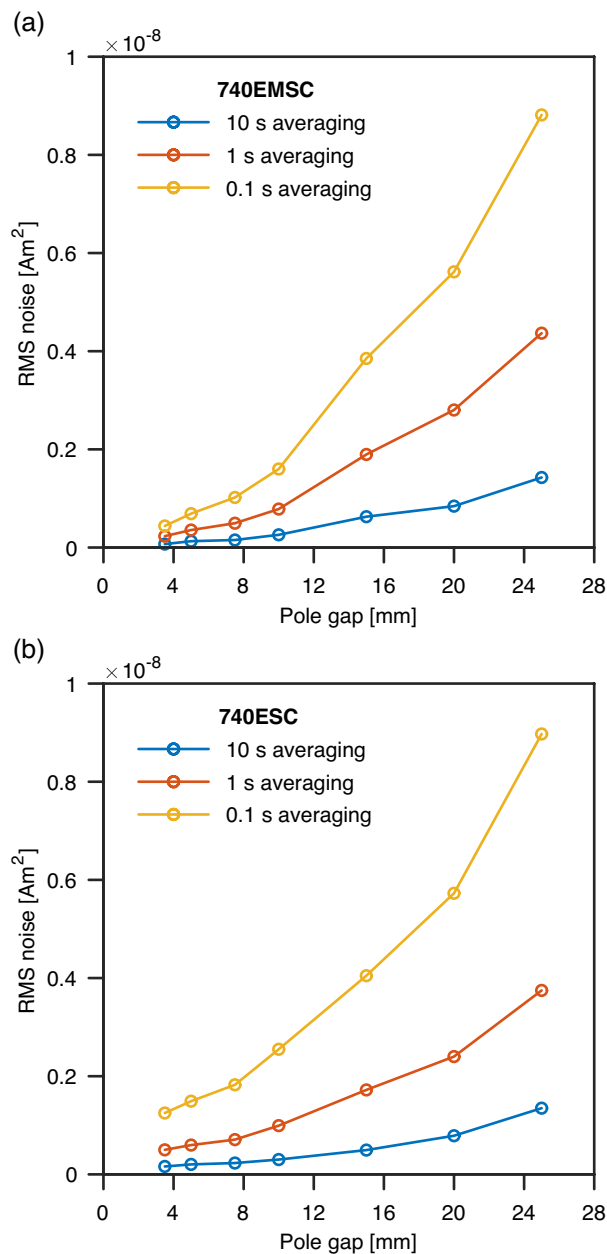
121 One of the most obvious approaches to increase the moment signal of a hysteresis loop is to
122 measure a larger specimen. For a specimen with uniformly concentrated magnetic particles,
123 increasing the volume by a factor n increases the magnetic moment by a factor n . A typical VSM
124 specimen is a small cylindrical core or gel capsule specimen with a diameter of 4–5 mm and height
125 of 5–6 mm (volume $\approx 0.125 \text{ cm}^3$). For weakly magnetized materials (e.g., carbonate sediment or
126 chert), however, this size may not be sufficient to obtain data of sufficient quality for analysis. To
127 produce a moment increase of a factor 10 requires increasing specimen dimensions by a factor of
128 $\sim 2.15 \left(\sqrt[3]{10}\right)$ to a size of $\sim 11 \text{ mm}$ (volume $\approx 1.3 \text{ cm}^3$). A limiting factor with increasing specimen size
129 is the specimen mass. A typical VSM has a mass limitation on the order of $\sim 10 \text{ g}$ and specimens
130 that are heavier than this may introduce noise to the vibration system and, ultimately, can lead to
131 failure of the vibration mechanism or damage the system and introduce a permanent and
132 undesirable source of noise. For a typical lithified sediment with a density of $\sim 2.2\text{--}2.8 \text{ g/cm}^3$, this
133 mass restriction corresponds to a maximum volume of $\sim 3.5\text{--}4.5 \text{ cm}^3$, or an equidimensional size of
134 $\sim 15\text{--}17 \text{ mm}$ – a factor $\sim 40\text{--}50$ increase in moment compared to the typical 4–5 mm specimen. For
135 powdered specimens, larger volumes can be used (lower density material), or the powder can be
136 more tightly compressed to increase the measurable mass, but packing too tightly may introduce
137 unwanted magnetostatic interactions (Chen et al., 2005). A caveat to increasing specimen size is
138 that this limits the minimum distance between the pick-up coils used to measure the specimen
139 moment – a larger specimen requires a large spacing, which reduces the overall moment
140 sensitivity of the system.

141 Most VSM systems have adjustable spacing between the pick-up coils used to detect the magnetic
142 moment of a specimen, known as the pole or air gap. This adjustment not only allows for variable
143 sizes of specimens to be measured, but offers higher moment sensitivity as well as higher applied
144 fields for smaller pole gaps. Pole gaps can typically range from 3.5 mm to 25 mm, and although
145 smaller and larger gaps are possible, they present problems in the form of physical interference
146 with specimen holders and practical limits on moment sensitivity, respectively. In **Figure 2** we re-
147 plot moment root mean square (RMS) noise as a function of pole gap spacing for the Lake Shore
148 7400 series VSMs (Dodrill, n. d.). Increasing the pole gap from $\sim 7\text{--}8 \text{ mm}$ (the minimum gap

149 suitable for a 4–5 mm specimen) to ~14 mm to accommodate a 10 times increase in volume would
150 result in a 2–4 times increase in the moment noise, irrespective of the measurement averaging
151 time. Although this source of noise can vary from system to system, increasing the size of the
152 specimen can yield a stronger signal without an overly large loss of moment sensitivity due to a
153 wider pole gap.

154 As a general rule of thumb, ~5 mm chips or cores are sufficient for most volcanic materials and
155 ~10 mm diameter gel caps (~1.4 cm³) hold enough material to measure many powdered
156 sediments. For weaker materials, 4 cm³ (~16 mm diameter) paleomagnetic cubes can be used.
157 These are smaller than typical paleomagnetic cubes (8 cm³), but allow the maximum possible
158 material volume while not overloading the VSM drive system. In some cases, however, measuring
159 a larger specimen may be not possible (e.g., insufficient material) and other methods of noise
160 reduction may be needed.

161 An alternative way to improve hysteresis signal-to-noise is to increase the measurement averaging
162 time, which is the duration over which each moment measurement is averaged. The MicroMag
163 3900 VSM has a sampling rate of 1 measurement per 10 ms and is capable of averaging over
164 times of 10 ms to 10,000 s (averaging 1 to 10⁶ measurements). In general, however, averaging
165 times less than 1 s, most commonly less than 500 ms, are sufficient for measuring a hysteresis
166 loop on a typical geological material. In Figure 3a we show a hysteresis loop measured in
167 continuous field sweep mode (described below) with an averaging time of 100 ms and in Figure
168 3b, we show the same specimen measured in continuous mode with a 200 ms averaging time. By
169 doubling the averaging time, we reduce the RMS noise curve by a factor of 1.66 (~ $\sqrt{2}$). Thirty
170 replicates of these measurements, confirm the $\sqrt{2}$ reduction in the average noise (average RMS
171 noise ratio of 1.51), which is expected if measurement noise is approximately independent and
172 identically distributed (i.i.d.) Gaussian noise. This level of noise reduction is a general feature of
173 increasing averaging time, such that increasing the averaging time by a factor n corresponds to
174 $\sim\sqrt{n}$ reduction in noise, but increasing measurement time by a factor n . The slightly higher level of
175 noise reduction we observe (1.51 versus 1.44) is likely a consequence of smoothing introduced
176 during necessary interpolation of the hysteresis loop data (see Section 4).



178

179 **Figure 2. Moment root mean square (RMS) noise as a function of the gap between the pick-**
 180 **up coils of the Lake Shore 7400 series VSM when measured with different averaging times.**

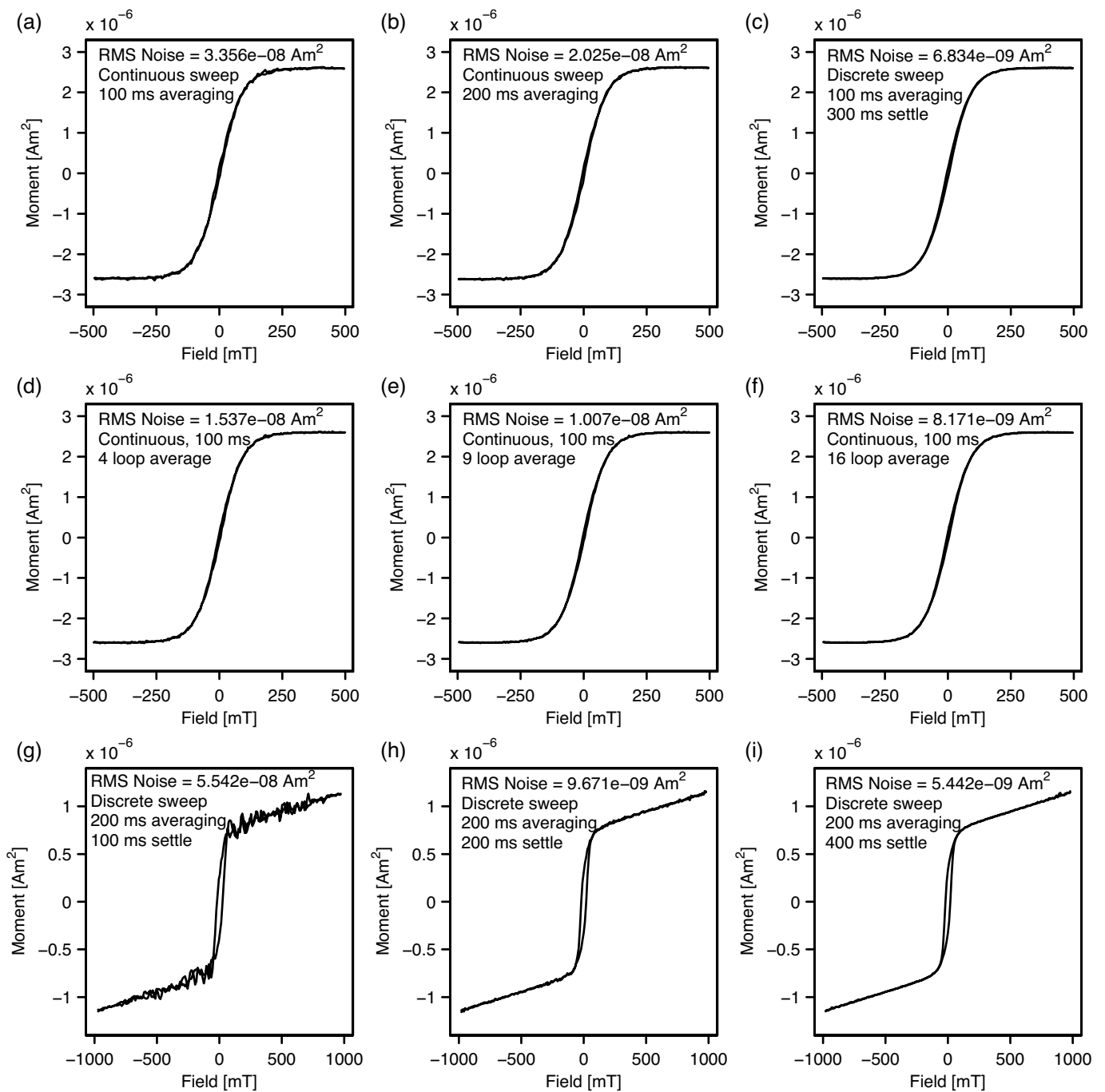
181 (a) The 740EMSC VSM, which is optimized for small specimens. (b) The 740ESC VSM. Data are
 182 from Dodrill (n. d.).

183

184 Another measurement setting that can be adjusted is the field sweep mode, which offers two
 185 possible options: continuous or discrete. Using continuous sweep mode, the field is swept over the

186 measurement averaging time and the average field and moment are recorded. In discrete mode
187 (also known as point-by-point mode), the field sweep is paused for a specified time (called the
188 pause or settling time) to allow the field to stabilize before the measurement proceeds. Continuous
189 mode offers a rapid measurement option that works well for strong specimens or where the field
190 sweep rate is low. For weaker samples, discrete mode often offers a higher signal-to-noise, but
191 with a longer measurement time. In Figure 3c, we show an example of a loop measured in discrete
192 mode with an averaging time of 100 ms and a settling time of 300 ms (i.e., the field is paused for
193 300 ms before the field and moment are averaged over the proceeding 100 ms). Compared with
194 the equivalent loop measured in continuous mode (Figure 3a), we see a reduction of noise by a
195 factor of 4.9 (30 replicates yield an average RMS noise reduction by a factor ~ 5), but with a factor
196 ~ 4.6 increase in measurement time. For weak specimens, measurement in discrete mode often
197 offers a better trade-off between improved signal-to-noise and increased measurement time (factor
198 $\sim n$ increase in time yields a factor $\sim n$ decrease in noise) than simply increasing the averaging time
199 (factor $\sim n$ increase in time yields a factor $\sim \sqrt{n}$ decrease in noise). The magnitude of noise
200 reduction switching from continuous to discrete field sweep depends not only on the choice of
201 averaging and settling times, but also on the exact shape of the loop – Hysteresis loops with large
202 gradient changes will benefit more from discrete sweep measurements.

203



204

205

206

207

208

209

210

211

212

213

Figure 3. Examples of hysteresis loops with differing measurement parameters and the resultant noise levels. Hysteresis loops from a volcanic speck measured with a continuous field sweep with a (a) 100 ms averaging time and (b) a 200 ms averaging time. The hysteresis loops measured using a discrete field sweep with a 300 ms settling time before measuring with a 100 ms averaging time. The average of (d) 4, (e) 9, and (f) 16 loops measured in continuous mode with 100 ms averaging. A cultured magnetotactic bacteria specimen (Li et al., 2012) measured in discrete mode with 200 ms averaging time and (g) 100 ms, (h) 200 ms, and (i) 400 ms settling time.

214 Another approach to improving signal-to-noise ratio is to average multiple hysteresis loops. To do
215 this, it is often, but not always, necessary to correct for measurement drift between each loop
216 before averaging (for our example data it is necessary and the drift is described in Section 3.2).
217 After correcting for inter-loop drift, we take the specimen shown in Figure 3a, and average it with a
218 total of 4, 9, and 16 loops (Figure 3d–f). This averaging requires interpolation of all loop moments
219 onto the same field spacing as the loop in Figure 3a. Although this interpolation adds a degree of
220 smoothing, the noise reduction by averaging n loops broadly follows the expected $\sim\sqrt{n}$ factor
221 reduction (noise is reduced by a factor 2.2, 3.3, and 4.1, for averaging 4, 9, and 16 loops,
222 respectively). Like increasing the averaging time, averaging n loops comes with a factor n increase
223 in the total measurement time. It should be noted, however, that to measure these 16 loops in
224 continuous sweep mode with 100 ms averaging, took approximately 720 s (with 402 points per
225 loop). A similar, or slightly lower noise can be achieved by using the discrete sweep mode with 100
226 ms averaging and 300 ms settling time, which requires just a single loop measurement time of only
227 ~ 210 s (compare Figure 3c and Figure 3f). Again, measuring in discrete mode often offers a better
228 trade-off between improved signal-to-noise and increased measurement time.

229 When measuring in discrete mode, the field settling time offers another means of reducing
230 measurement noise. In Figure 3g–i, we compare three loops measured in discrete mode with an
231 averaging time of 200 ms and settling times of 100, 200, and 400 ms. We observe that a factor n
232 increase in settling time results in a factor $\sim n^2$ reduction in the loop RMS noise (confirmed by
233 additional measurements at 100 and 300 ms averaging). This large reduction in noise rapidly
234 approaches the manufacturer’s nominal moment sensitivity of $\sim 0.5 \times 10^{-9} \text{ Am}^2$ (1000 ms averaging,
235 pole gap unspecified), and in our collective experience, settling times of > 500 ms offer little
236 improvement at the expense of considerably longer measurement times. Generally, settling times
237 of 100–300 ms are sufficient for most measurements.

238 Overall, for weak and noisy hysteresis loops, measuring in discrete field sweep mode with
239 averaging times of 100–300 ms and settling times of ~ 300 ms offers the best balance between
240 maximizing signal-to-noise, while maintaining a reasonable measurement time (hence minimizing
241 drift). Each specimen and instrument is, of course, unique, and each measurement should be

242 tailored appropriately. For example, chips of volcanic materials that are > ~2–3 mm in size are
243 typically strong enough to be measured in continuous mode with short (~100 ms) averaging times
244 – The example in Figure 1 is a such a chip, but has a RMS noise of $\sim 1 \times 10^{-8} \text{ Am}^2$, or < 0.05% of the
245 saturation moment (M_s), while the example in Figure 3a has a RMS noise of ~1.3% of M_s . The
246 above descriptions of loop noise and guidelines for reduction should serve as general starting point
247 for the majority of specimens encountered by the rock and paleomagnetic community.

248 **3.2 Minimizing drift**

249 Although the sources of drift can be difficult to characterize and quantify, many can be related to
250 temperature or mechanical effects. Thermal factors are relevant not only to the temperature of the
251 specimens being measured, but also to the ambient temperature of the room and to temperature
252 changes of the experimental apparatus as the experiments proceed. Mechanical factors can be
253 related to the solidity/friability of the specimen, specimen position during measurement, or the
254 physical mechanisms and electronics of the instrument being used.

255 Temperature changes in the specimen being measured are one potential source of thermal drift.
256 Not only can this affect measurement of the temperature dependence of magnetic properties, but
257 can also have an impact on measurements at room temperature due to the temperature between
258 the pole pieces being influenced by the temperature of the magnets. This type of thermal drift can
259 strongly influence specimens with large paramagnetic components such as sediment samples and
260 is most likely the main cause of extreme drift and failure of loops close after return to the initial
261 saturation field.

262 This drift type of thermal drift, which we term paramagnetic drift, can be described by a simple
263 temperature model of paramagnetic moments (Jackson and Solheid, 2010). Curie's Law states
264 that the paramagnetic magnetization (M_p) in an applied field, B , is inversely proportional to
265 temperature, T :

$$266 \quad M_p(B, T) = \frac{CB}{\mu_0 T}, \quad (1)$$

267 where C is the Curie constant and μ_0 is the permeability of free space. If the temperature of a
268 specimen changes from an initial temperature of T_0 to temperature T_i , the paramagnetic
269 magnetization at can be expressed as:

$$270 \quad M_p(B, T_i) = M_p(B, T_0) \frac{T_0}{T_i}. \quad (2)$$

271 Here T_i follows Newton's Law of Cooling:

$$272 \quad T_i = T(t_i) = T_A + (T_0 - T_A) \exp(-kt_i). \quad (3)$$

273 where T_A is the ambient temperature (temperature between the VSM pole pieces), k is a rate
274 constant, and t_i is the time of the i^{th} measurement.

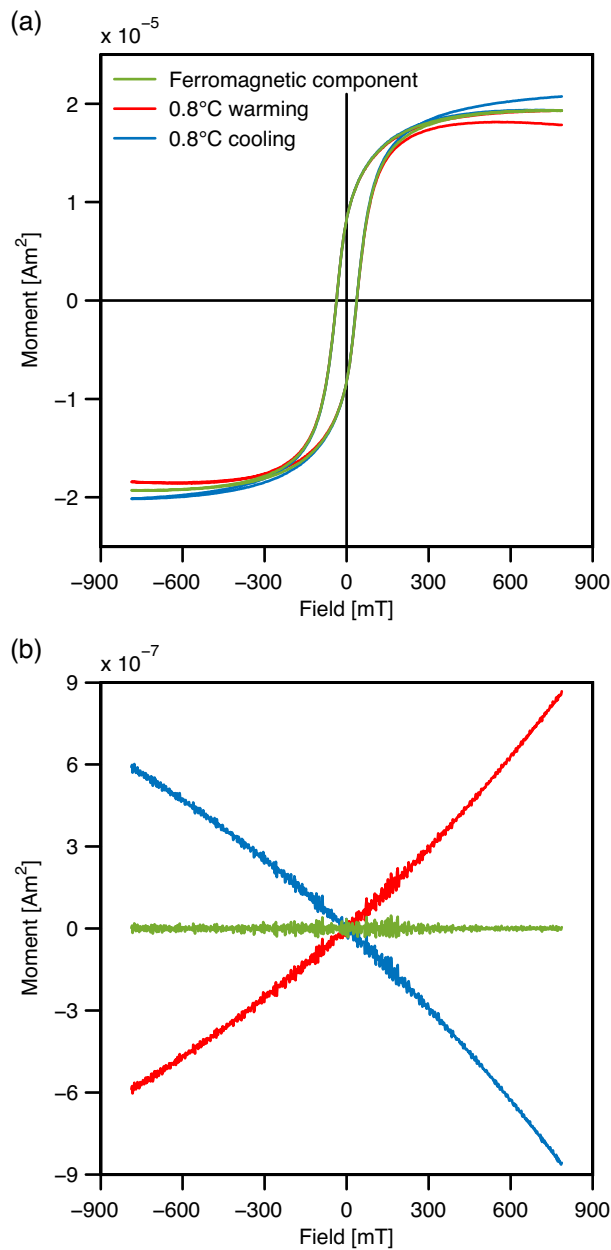
275 In **Figure 4** we show examples of hysteresis loops that experience drift due to a change in
276 temperature inducing a change in paramagnetic magnetization. Here we take the ferromagnetic
277 loop shown in Figure 1 and add in a paramagnetic contribution such that in a 1 T field the ratio of
278 paramagnetic to ferromagnetic magnetization (M_p/M_f) is 35 (many natural sediments have ratios of
279 ~ 1 to > 50). The initial specimen temperature is set to 20°C and we model two loops where the
280 ambient temperature is initially 1.5°C above and below the specimen temperature, such that the
281 specimen experiences warming and cooling, respectively. All loops, therefore, start at the same
282 point (**Figure 4**). The rate constant in equation 3 is set such that the specimen does not reach
283 thermal equilibrium, but experiences a 0.8°C temperature change over the measurement of each
284 loop. All loops have been corrected for the paramagnetic contribution using the known high-field
285 paramagnetic susceptibility.

286 The green loop in **Figure 4a** is the loop that would be measured if there is no change in the
287 specimen temperature (i.e., specimen and ambient temperatures are the same). If the ambient
288 temperature is initially above specimen temperature, then the specimen experiences warming
289 towards ambient and the loop fails to close after returning to positive saturation with the lower
290 branch lying well below the upper branch (red loop **Figure 4a**). The apparent M_s value after high-
291 field slope correction is lower than the true value. If the specimen is initially above ambient
292 temperature and experiences cooling towards ambient, the lower branch crosses the upper as the

293 loop returns to positive saturation and ends well above the upper branch (blue loop **Figure 4a**).
294 The apparent M_s value, however, is higher than the true value. This lack of closure can be
295 quantified by a closure error (M_{ce}), which is the difference between the moments of initial and final
296 peak positive field measurements. In both cases M_{ce} is $\sim 7.5\%$ of the true M_s value.

297 This type of drift always manifests as failure of the loop to close (**Figure 4a**) and a non-linear noise
298 curve (**Figure 4b**). These features, however, can be variable as they are dependent not only on
299 the relative strength/abundance of paramagnetic minerals with respect to the ferro-/ferrimagnetic
300 contribution, but also on the initial temperature of the specimen, ambient temperature, as well as
301 the thermal properties of the specimen, which control k in equation 3.

302 This kind of thermal drift can be minimized by a number of simple steps to control temperature
303 fluctuations. Among other measures, this can include regulating room temperature with the use of
304 air conditioning, ensuring laboratory doors are closed to prevent uneven temperatures, shading
305 windows to avoid heating by sun glare, and minimizing the temperature difference between room
306 temperature and the water used to cool the electromagnets (but maintaining appropriate operating
307 temperature). Similarly, allowing a specimen to thermally stabilize before measurement will reduce
308 drift, particularly if temperature dependent hysteresis loops are being measured. Even for room-
309 temperature measurements this effect can be important if the cooling-water temperature and
310 temperature in the magnet air gap differ significantly from the general room temperature. In such
311 cases it is beneficial to allow the samples to thermally equilibrate on the electromagnet base prior
312 to measurement. As noted before, thermal drift has the strongest influence on specimens that have
313 large paramagnetic contributions with respect to the ferromagnetic component. So, these
314 precautions may not be needed for all types of specimens.



315

316 **Figure 4. Theoretical model of paramagnetic thermal drift.** (a) Example hysteresis loops of a
 317 theoretical ferromagnetic component mixed with a strong paramagnetic component that
 318 experiences thermal drift during measurement. The green loop is the expected loop if the
 319 specimen experiences no temperature change during measurement. The red and blue loops are
 320 for a specimen that experiences warming and cooling towards ambient temperature, respectively,
 321 during measurement. All loops have been corrected for the known high-field paramagnetic
 322 susceptibility. (b) The resultant noise curves. Colors are the same as in part (a).

323

324 Drift can also be caused by non-thermal mechanisms. This can include instabilities in the vibration
325 system, electronic drift, or physical movement of the specimen during measurement. Quantifying
326 the manifestation of these types of drift is difficult and, depending on the source, may be a linear or
327 non-linear function of time and/or field. Avoiding extremely heavy specimens, ≥ 10 g, which are at
328 or beyond the specifications of the VSM system being used, can minimize vibrational drift and
329 prevent long-term damage. Physical movement of the specimen during measurement can occur if
330 it is not properly attached to the holder or if a powder is not properly compacted.

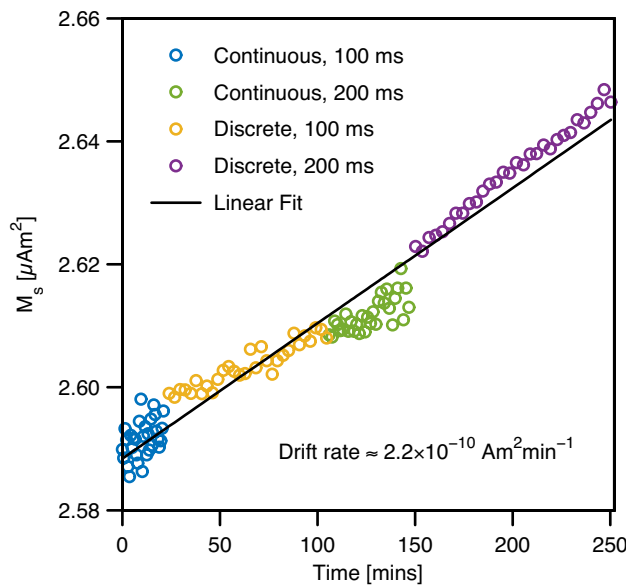
331 For the 30 replicates of each loop shown in **Figure 3a–c** (plus 30 replicates of the loop measured
332 in discrete mode with 200 ms averaging and 300 ms settling time; a total of 120 loops), the total
333 measurement time for these 120 loops was ~ 250 minutes. Over this time, we observe an
334 approximately linear increase in M_s of $\sim 6.3 \times 10^{-8} \text{ Am}^2$ ($\sim 2.4\%$ of the average M_s value), which
335 corresponds to a drift rate of $\sim 2.2 \times 10^{-10} \text{ Am}^2 \text{ min}^{-1}$ (

336 **Figure 5**). Drift for the longest individual loop measurements of ~ 210 s (discrete field sweep with
337 200 ms averaging) is on the order of 0.02% of M_s and can be neglected. This specimen was a
338 speck of basalt (< 1 mg) mounted to the VSM sample holder using silicon grease and although this
339 drift is small, this is an example of mechanical drift related to changes in the specimen's position
340 during measurement. Such movement can be avoided by properly fixing the specimen to the
341 holder.

342 For solid specimens, glue can be easily used to affix the specimen to the holder, but allow
343 sufficient time for the glue to dry otherwise the specimen may fall off during measurement. We
344 recommend the use of water-based polyvinyl acetate (PVA) glue (superglue can easily damage
345 friable specimens and is harder to remove from the holder). For powdered specimens packed into
346 gel caps or cubes, an additional top layer of cotton wool can help better compact the specimen and
347 avoid particle movement. In extreme cases, the powder can be impregnated with glue to solidly
348 bind the particles, but this is generally not needed.

349

350



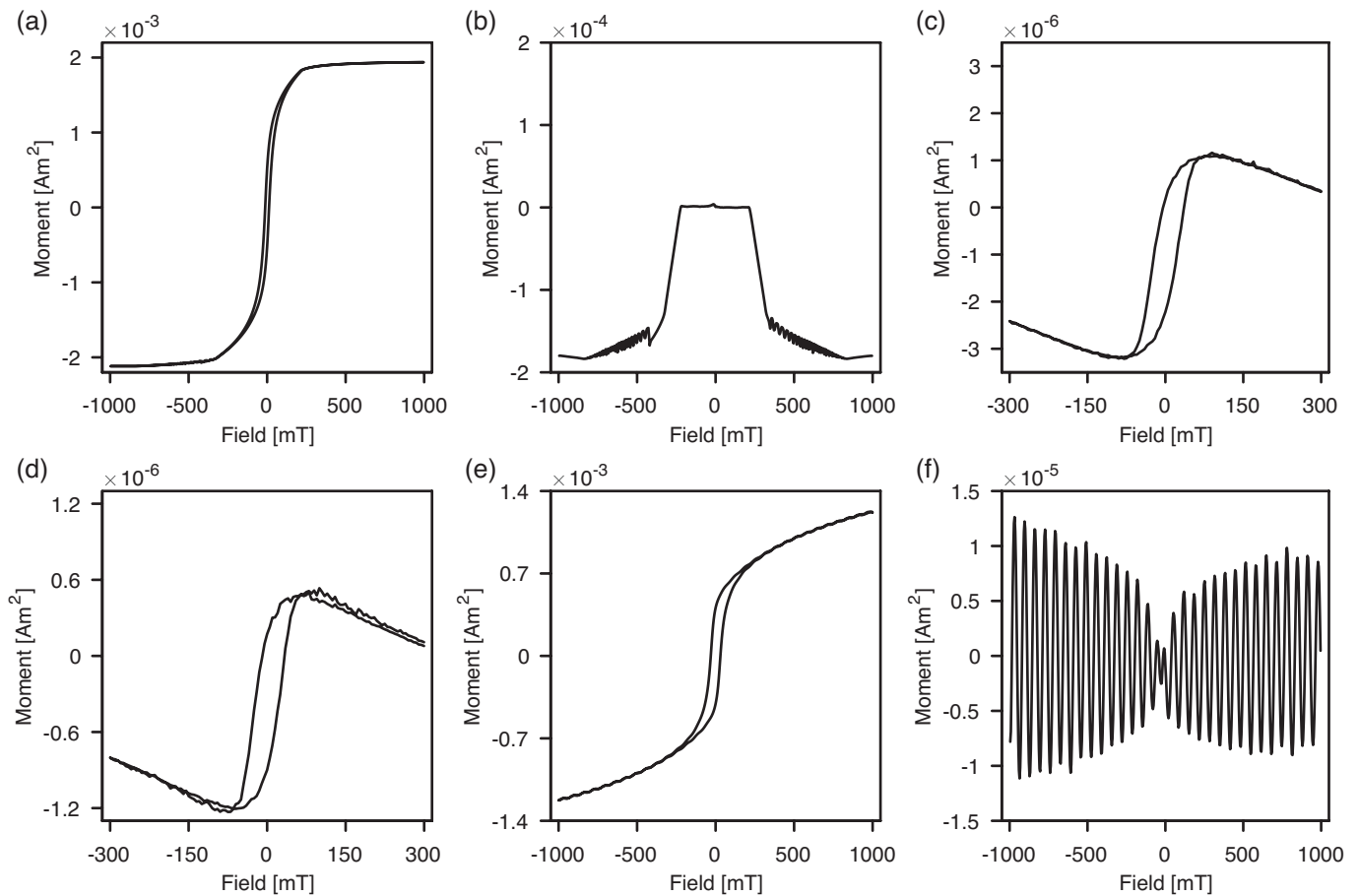
351

352 **Figure 5. Moment drift caused by specimen movement over time.** Change in saturation
 353 moment over the ~250 mins needed to measure the 120 loops comparing averaging times and
 354 continuous and discrete field sweep modes.

355

356 3.3 Other influences

357 Instruments for measuring hysteresis loops typically have nominal moment ranges of $\sim 10^{-11}$ – 1 Am^2
 358 and specimens weaker or stronger than this cannot be easily measured. For a MicroMag 3900
 359 VSM (nominal moment range of 5×10^{-8} – $1 \times 10^{-2} \text{ Am}^2$), the moment range (“sensitivity” setting) has
 360 to be selected manually. The VSM software warns if the range is set too low for the specimen
 361 moment, but if missed incorrect moment range can have a detrimental impact on the loop
 362 measurement. This can easily happen if the high-field slope is negative and the peak moment
 363 occurs at low fields (cf. Figure 6c), or when the loops are measured as a function of temperature
 364 and the specimen moment increases beyond the initially set range. Figure 6a is an example of a
 365 loop measured with the moment range set too low. The high-field branches have a distinct change
 366 in slope that does not follow the natural curvature of the loop. For other specimens, this effect may
 367 occur subtly at higher fields and may give the impression of reaching saturation. The noise curve
 368 (Figure 6b) has a distinct plateau shape that is characteristic of the moment range being too low
 369 and can be diagnostic when the effects are subtle.



370

371 **Figure 6. Examples of hysteresis loops suffering from other detrimental effects.** (a) A
 372 hysteresis loop measured with the moment range set too low. (b) The noise curve of the loop
 373 shown in part (a). (c) A hysteresis loop offset from the plot origin due to the presence of an
 374 electrostatic charge on the specimen holder. (d) A specimen with an electrostatic charge that
 375 partially dissipated during measurement. (e) A hysteresis loop that suffers from vibrational
 376 instability. (f) The noise curve of the loop shown in part (e) reveals a clear periodicity to the noise.
 377 The loop in parts (e) and (f) is a volcanic chip from Muxworthy et al. (2011).

378

379

380 Some systems are capable of dynamically adjusting the moment range and such artifacts are not
381 an issue. Where the range has to be set manually, the range should be set prior to measurement
382 with the specimen in place and most commonly with the peak measurement field applied. In some
383 cases, however, if the specimen is has a strong diamagnetic component and a negative high-field
384 slope, the maximum moment in the loop measurement occurs at lower fields and a large portion of
385 the loop will need to be measured before an incorrect moment range is detected. Data with the
386 moment range set too low must be remeasured to obtain interpretable data.

387 Most VSMS will allow the vibration amplitude to be adjusted. Reducing the vibration amplitude
388 reduces the magnitude of the voltage induced in the pick-up coils and allows the moment
389 sensitivity to be adjusted to a higher range. If the moment range is set to the instrument maximum
390 and this effect still occurs, the specimen is too strong and should be reduced in size then
391 remeasured. Alternatively, if reducing sample size is undesirable, a wider pole gap may allow
392 measurement (a wider pole-gap reduces the magnitude of the voltage induced in the pick-up coils;
393 note that the system should be recalibrated if the gap is adjusted).

394 In Figure 6c we show an example of a hysteresis loop from a magnetotactic bacteria (MTB)
395 specimen deposited in a plastic cube (Paterson et al., 2013). The loop is offset from the plot origin
396 due to an electrostatic charge on the plastic cube. Such oscillating electrostatic charges are
397 equivalent to time-varying currents, which generate changing magnetic fluxes that are additive to
398 that from the specimen moment, and typically manifest as a large moment offset with negligible
399 field offset. The electrostatic signal is independent of applied field, which preserves the size and
400 shape of the loop and allows for correction of the offset (see Section 4.2).

401 Figure 6d is a hysteresis loop from another MTB specimen in a plastic cube with an electrostatic
402 charge. In this example, the static charge partially dissipates during measurement causing the
403 lower branch to lie above upper branch on returning to positive saturation. The various methods
404 used to correct for loop drift (outlined in Section 4.4) perform poorly for this type of drift and such
405 loops are best remeasured (the distribution of moment drift depends on when and how fast the
406 charge dissipates). Anti-static sprays can help dissipate electrostatic fields before measurement. In

407 laboratories where electrostatic charges are a long term problem (e.g., locations with seasonal
408 periods of low humidity), air ionizers can be used to reduce the build-up of static charges.

409 On VSMS, the vibration drive system can also be a source of noise. Figure 6e is an example of
410 loop that suffers from vibrational drive instability. Examination of the noise curve (Figure 6f) reveals
411 that the noise is highly periodic and a spectral analysis (not shown) indicates significant power at
412 an angular frequency of 1.84 Hz, confirming that this is not random noise. The exact cause of this
413 periodic noise is unknown, but is likely due to instability in the electronic feedback loop that
414 controls the vibration drive system (H. Reichard, personal communication, 2018). Although
415 observable, in this case, the magnitude of the instability is insufficient to greatly affect the
416 interpretation of the loop statistics.

417 Other possible sources of vibrational drive instability include insecure drive rods, loose specimen
418 holders or specimens not being fully secured to the holder, the specimen touching the pole pieces
419 or Hall probe, or noise introduced by overloading the system with heavy (> 10 g) specimens. For
420 mechanical sources of instability, simple fixes of securing drive rods and specimens, and ensuring
421 vibrations are unimpeded will resolve any noise issues. Particular attention should be paid to
422 ensure the specimen does not physically interact with Hall probe as this may damage the
423 probe. For the case of periodic instability (Figure 6e, f), restarting the instrument, reseating the
424 vibration drive system cables, and adjusting the orientation stage have been known to resolve this
425 issue. If these simple approaches fail to remove vibrational drive instability, users should consult
426 the instrument manufacturers for further advice.

427

428 **4 Hysteresis processing**

429 Following measurement of a hysteresis loop it is necessary to process the data appropriately to
430 correct for unavoidable negative influences (e.g. unavoidable drift etc.) and isolate the desired
431 components before extracting the parameters and statistics of interest for further analysis. To that
432 end, we have developed new graphical software called *HystLab* to aid the paleo- and rock
433 magnetic community in processing and analyzing hysteresis loop data. The remainder of this

434 paper will discuss the functionality of *HystLab* and the tools available to minimize the detrimental
435 impact of measurement artifacts on the final interpretation of hysteresis data.

436 *HystLab* supports a number of advanced processing options that are combined with automated
437 decision processes used by default for all specimens when they are first loaded. This includes
438 automatic centering of hysteresis loops and automatic decisions on drift and saturation slope
439 corrections (details outlined below). In general, this default processing performs well for most
440 geological specimens and provides a quick starting point for users to analyze their data. The
441 default processing, however, may not be suitable for every specimen. We therefore strongly
442 encourage analysts to carefully consider the processing of each specimen to ensure
443 appropriateness.

444 **4.1 Loop interpolation**

445 All hysteresis processing in *HystLab* is based around the assumed symmetry of the basic
446 hysteresis loop and the remanence and induced hysteretic curves. When comparing the upper and
447 lower branches it is necessary to interpolate to consistent field steps. When a “raw” hysteresis loop
448 is initially processed and analyzed, the lower branch is inverted and linearly interpolated to the field
449 steps of the upper branch. For all other processing, both the upper and lower branches are linearly
450 interpolated on to a regularly spaced field grid. To avoid extrapolation of data where there are no
451 measurements, the peak field of the grid is taken as the lowest of the four absolute peak fields
452 (termed B_{max}). To avoid artificially oversampling the loop, the number of points used, n , is taken to
453 be the minimum number of points used to measure either the upper or lower branches (after fields
454 with absolute field values $< B_{max}$ are removed). The interpolation field grid is n equally spaced field
455 points in the range $[B_{max}, -B_{max}]$. These necessary interpolations inevitably introduce a degree of
456 data smoothing and as a result, estimates of noise and loop quality statistics (described below) are
457 likely to be slight underestimates and overestimates, respectively, of their true values.

458 **4.2 Loop centering**

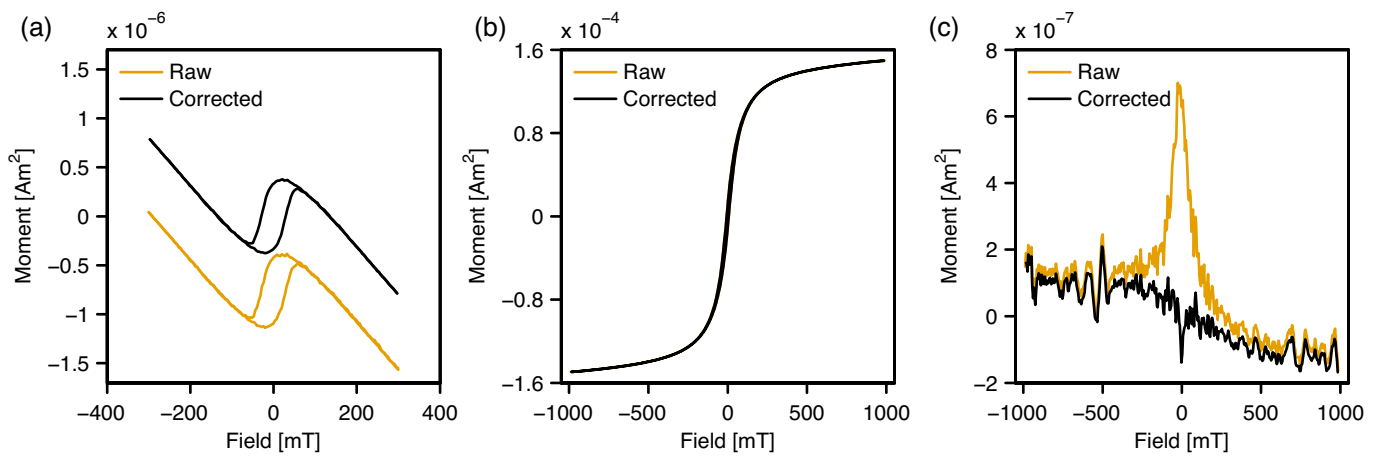
459 If uncorrected, asymmetry of a loop about the origin may lead to misestimating of hysteresis
460 descriptive statistics (e.g., M_s , M_{rs} , B_c , etc.). In Figure 7a we show an example of extreme loop

461 offset of a magnetotactic bacteria specimen with a strong diamagnetic signal from the specimen
462 holder (Paterson et al., 2013). This large moment offset (on the order of the specimen's M_s) is
463 likely caused by an electrostatic charge on the specimen's plastic holder. A subtler example of loop
464 offset is seen from a volcanic specimen from Paterson et al. (2010) (Figure 7b). This less visually
465 obvious offset becomes evident in the noise curve where it manifests as a distinct peak around
466 zero field (Figure 7c). This peak is removed and the root mean square noise level is reduced by a
467 factor two after correctly centering the hysteresis loop (Figure 7c). Following loop centering, a
468 systematic trend in the noise curve becomes more evident (Figure 7c) – This is due to
469 measurement drift (drift corrections are discussed in Section 4.4).

470 Loop offset is corrected for following Jackson and Solheid (2010), whereby the offset along the
471 field axis is found by maximizing the linear correlation between upper branch and inverted lower
472 branch when the lower branch is shifted by the correct field offset (B_0). The intercept of a linear
473 model fit to the B_0 shifted lower branch and upper branch corresponds to twice the offset along the
474 moment axis (M_0).

475 In *HystLab*, a Nelder-Mead optimization routine (Lagarias et al., 1998) is used to find the correct
476 field offset. For determining the moment offset, we employ a major axis regression model, which,
477 given the lack of obvious choice of dependent and independent variables (upper versus lower
478 branch moments) and the likely similar noise structure of the upper and inverted lower branches, is
479 more appropriate than a standard linear regression model.

480



481

482 **Figure 7. Examples of specimens requiring loop centering.** (a) A magnetotactic bacteria
 483 specimen with visually obvious loop offset (Paterson et al., 2013). (b) A volcanic specimen
 484 (Paterson et al., 2010) with more subtle offset, which is evident as a zero-field spike in the noise
 485 curve (c) that is removed after loop centering. RMS noise is 3.679×10^{-6} Am² before correction and
 486 1.907×10^{-6} Am² after.

487

488

489 4.3 Loop quality

490 The squared linear correlation (R^2) between the upper and inverted lower branches can be used to
 491 define a quantitative measure of the quality (Q) of a hysteresis loop (Jackson and Solheid, 2010).
 492 The definition of Q used in *HystLab* is given by:

$$493 \quad Q = \log_{10} \left(\frac{1}{\sqrt{1-R^2}} \right), \quad (4)$$

494 This differs from the definition of Jackson and Solheid (2010) who erroneously omitted the square
 495 root in the denominator in their paper; although it was included in their calculations and internal
 496 software at the Institute for Rock Magnetism, University of Minnesota, which has been used to
 497 quantify numerous hysteresis loops. Q values in *HystLab* take the square root to maintain
 498 consistency, and we view the above definition of Q as correcting that of Jackson and Solheid
 499 (2010).

500 In addition to the quality of the raw loop (Q) and the fully processed loop (Q_f), *HystLab* also
501 determines the quality of the remanent (Q_{rh}) and induced (Q_{ih}) hysteretic curves. These Q values
502 are based on the expected reflection and rotational symmetries of the remanent and induced
503 curves, respectively, and the correlations between the negative and positive field halves.

504 **4.4 Drift correction**

505 Given the diverse possible sources of hysteresis loop drift, a number of different approaches to
506 drift correction have been proposed and *HystLab* supports many of these. In addition to the option
507 of applying no drift correction, *HystLab* offers four types of correction: 1) positive field correction, 2)
508 upper branch correction, 3) symmetric averaging, and 4) paramagnetic drift correction. The
509 positive field correction subtracts the smoothed noise curve from the positive field segments of the
510 hysteresis loops: The positive field half of the noise is subtracted from the positive field half of the
511 upper branch and the negative field half of the noise curve (reflected to positive fields) is
512 subtracted from positive field half of the lower branch (Jackson and Solheid, 2010). The upper
513 branch correction subtracts the smoothed noise curve from the upper branch of the hysteresis loop
514 only (Jackson and Solheid, 2010). Symmetric averaging follows von Dobeneck (1996), whereby
515 the upper and inverted lower branches are averaged and vertically shifted by half their tip-to-tip
516 separation to ensure loop closure; This results in a zero noise curve. The paramagnetic drift
517 correction accounts for changes in paramagnetic moment due to changes in specimen
518 temperature and is described in detail below.

519 An automatic correction option is available, which decides between positive field and upper branch
520 corrections. The decision is based on the ratio of drift in the high-field range ($\geq 75\%$ of the peak
521 field) to the low-field range. If drift tends to occur in the high-field range then the positive field
522 correction is applied, otherwise the upper branch correction is applied. In most cases, the positive
523 field correction tends to perform best and is therefore favored in the automatic correction
524 approach. We note, however, that although these methods for drift correction generally recover
525 many statistics with reasonable accuracy, the detailed shape of the loop may not always be
526 accurately recovered for certain types of drift (e.g., paramagnetic thermal drift).

527 The paramagnetic drift correction is newly introduced here and is based on the thermal model of
528 paramagnetic drift described in Section 3.2, which after expansion, describes the change in
529 paramagnetic moment in terms of the ratio (T_r) of a specimen's initial absolute temperature (T_0) to
530 ambient absolute temperature in the measurement space (T_A): $T_r = T_0/T_A$. The first step of this
531 method is to correct drift using the positive field correction described above, and the user defined
532 high-field slope correction (see Section 4.5) is applied to estimate the high-field/paramagnetic
533 susceptibility (χ_{HF}). If no saturation slope correction is applied a linear fit is made to the data at
534 fields $\geq 70\%$ of the peak field (this slope correction is not applied to the final loop, but used only to
535 estimate χ_{HF}). This estimate of χ_{HF} is used to estimate the paramagnetic magnetization
536 ($M_p = \chi_{HF}\mu_0 B$). The thermal rate constant, k , and the relative temperature ratio T_r are then
537 optimized to fit the observed noise curve. Each point of the hysteresis loop is then corrected for the
538 predicted change in the paramagnetic moment. Following this, the above described automatic drift
539 correction routine is used to apply either a positive field or upper branch correction to account for
540 any other drift not related to paramagnetic thermal instabilities.

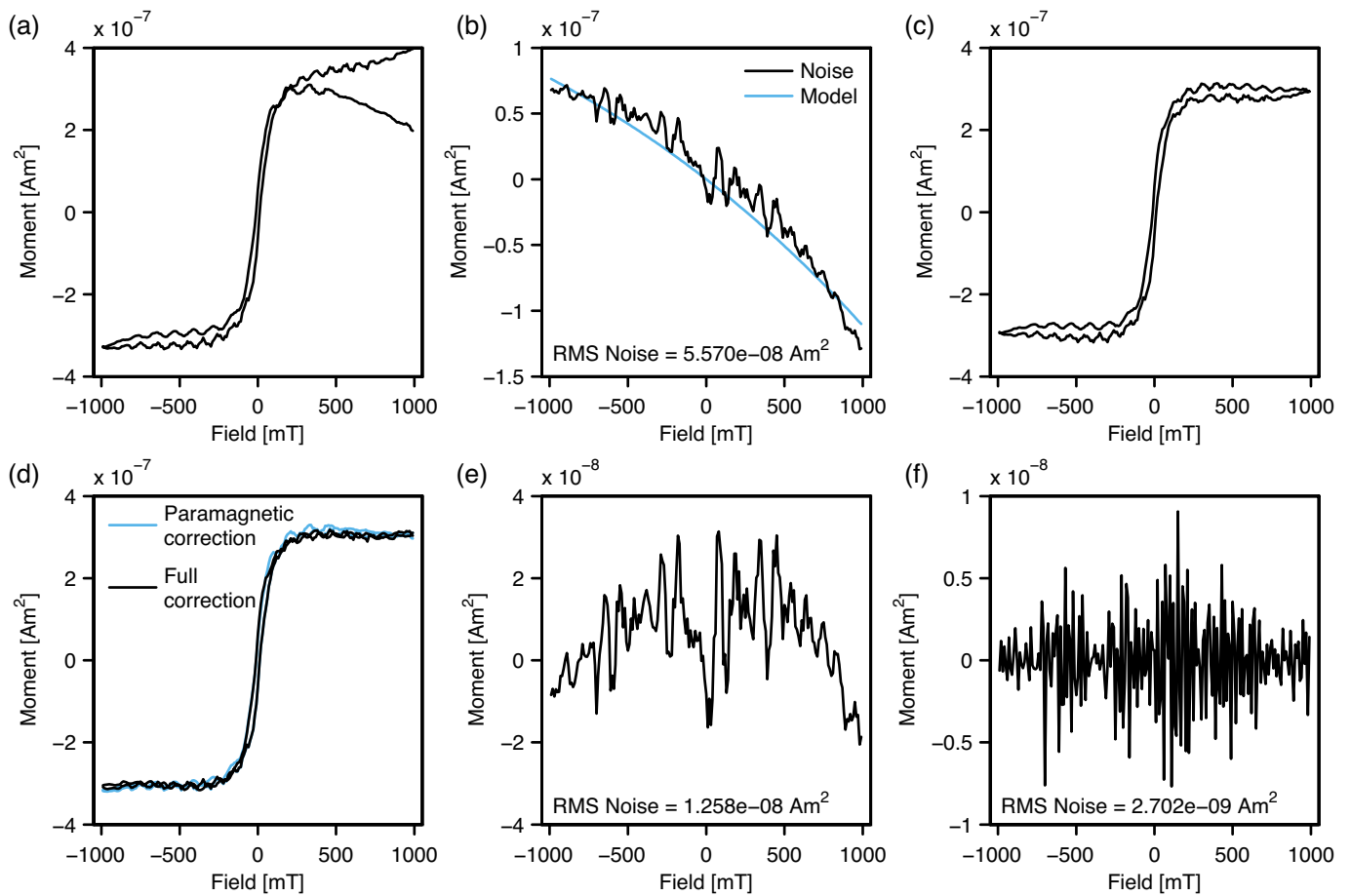
541 An advantage of this correction over others is that it provides a justifiable means of distributing
542 components of drift across all measurements and not just across a restricted range of data (e.g.,
543 positive fields only). Furthermore, for specimens that experience this type of thermal drift, the
544 hysteresis loop shape is generally better recovered than with the other corrections.

545 An example of a specimen with extreme paramagnetic drift is shown in Figure 8a. This specimen is
546 a relatively weak lake sediment with a ferromagnetic component dominated by detrital magnetite
547 (Liu et al., 2015). This specimen is strongly paramagnetic with a 1 T para-to-ferromagnetic
548 magnetization ratio (M_p/M_f) of ~ 35 (cf. the theoretical example in Section 3.2). After linear high-field
549 slope correction, the lower branch crosses the upper branch and lies well above the upper branch
550 resulting in a closure error of $M_{ce} = -1.993 \times 10^{-7} \text{ Am}^2$ ($\sim 65\%$ of the estimated M_s). The noise curve
551 is non-linear with an RMS of $5.570 \times 10^{-8} \text{ Am}^2$ or $\sim 18\%$ of M_s (Figure 8b). A positive field drift
552 correction reduces the closure error ($M_{ce} = -6.390 \times 10^{-10} \text{ Am}^2$; $\sim 0.2\%$ of M_s), yields more acceptable
553 saturation behavior, and reduces the RMS noise ($2.783 \times 10^{-9} \text{ Am}^2$, $\sim 1\%$ of M_s). Although this loop
554 looks more reasonable, the high-field portions are offset from each other and close only at the

555 peak fields, giving the impression of high coercivity “lobes” (Figure 8c). The shape factor (Fabian,
556 2003) of the loop is 1.47. This is indicative of extremely wasp-waisted behavior and the presence of
557 a high coercivity component, which is not seen in isothermal remanent magnetization acquisition
558 data and does not fit with the geological context of the specimen (Liu et al., 2015; Liu et al., 2016).
559 An upper branch correction fails to reduce the loop closure error and symmetric averaging
560 exaggerates the high coercivity lobes yielding a loop shape factor of 1.67.

561 The paramagnetic drift model fit to the noise curve is shown in Figure 8b and the paramagnetic
562 drift corrected loop in Figure 8d. The loop is considerably more closed than before correction (post-
563 correction $M_{ce} = -1.340 \times 10^{-8} \text{ Am}^2$) and the high-coercivity “lobes” seen in positive field corrected
564 loop are absent. Although after applying only the paramagnetic drift correction RMS noise is
565 reduced ($1.258 \times 10^{-8} \text{ Am}^2$), considerable structure remains in the noise curve, which indicates that
566 not all drift has been corrected for and another source of drift is likely present (Figure 8e). After
567 applying the paramagnetic drift correction followed by the upper branch correction, the RMS is
568 further reduced and becomes flat, which should be expected from random measurement noise.
569 The fully corrected loop (Figure 8d) changes only slightly, but both RMS noise ($2.702 \times 10^{-9} \text{ Am}^2$)
570 and the closure error are reduced ($M_{ce} = -6.700 \times 10^{-9} \text{ Am}^2$), yielding a much more reasonable
571 hysteresis loop that can be more easily interpreted. The shape factor for the fully corrected loop,
572 0.06, indicates a constrained coercivity population, which is more consistent with the geological
573 context of the specimen (Liu et al., 2015; Liu et al., 2016).

574



575

576 **Figure 8. Example of hysteresis loop drift and the paramagnetic drift correction.** (a) A weak
 577 lake sediment sample from Liu et al. (2015) where the loop fails to close after returning to positive
 578 saturation. (b) The noise curve (black line) exhibits a clear non-linear field dependent trend
 579 indicative of drift. This trend can be well modeled by a paramagnetic thermal drift model (blue line).
 580 (c) The hysteresis loop closes after positive field drift correction, but the overall shape of the high-
 581 field regions is not satisfactory and does not match the geological context of the specimen. (d) The
 582 hysteresis loop after paramagnetic drift correction only (blue loop) and after applying the combined
 583 paramagnetic and positive field drift correction (black loop). (e) After paramagnetic drift correction
 584 the RMS noise is reduced, but considerable structure remains in the noise curve, indicating other
 585 drift sources are present. (f) The noise curve is flat after the full drift correction.

586

587 The paramagnetic thermal drift model estimates a temperature ratio of 1.036 for this hysteresis
588 loop. At the Institute of Geology and Geophysics, Chinese Academy of Sciences (IGGCAS), where
589 this measurement was performed, the VSM electromagnets are cooled with chilled water running
590 at $\sim 17\text{--}19^\circ\text{C}$, which would yield an initial specimen temperature of $\sim 27\text{--}29^\circ\text{C}$. Although high for the
591 time of measurement (mid-May with typical daytime ambient temperatures on the order of $\sim 20\text{--}$
592 26°C), it is still plausible. The exact room and specimen temperatures were not measured, so we
593 cannot exclude the possibility of unusual temperature conditions such as sun glare warming, which
594 can occur. Similarly, we cannot exclude the possibility that the model may be fitting other
595 components of drift not related to paramagnetic thermal effects and this may skew the estimated
596 temperature ratio.

597 This paramagnetic drift correction is not suitable for all specimens and works best for those with a
598 distinct lack of loop closure and strongly non-linear noise curve (e.g., Figure 8a, b). For example,
599 applying this correction to the loop shown in Figure 7b (noise curve is given in Figure 7c), yields a
600 temperature ratio of ~ 1.19 . That is, the initial temperature of the specimen was $\sim 20\%$ higher than
601 ambient. For an ambient temperature of $\sim 293\text{ K}$ ($\sim 20^\circ\text{C}$) this estimates a specimen temperature of
602 almost 80°C , which is physically unreasonable and indicates that the drift is unlikely to be related
603 to paramagnetic thermal effects. When applying this type of drift correction these factors should
604 always be considered when assessing the physical plausibility of the model and correction.

605 **4.5 Saturation slope correction**

606 In sufficiently high magnetic fields, the moment of ferro- and ferrimagnetic materials saturates,
607 while the moments of para- and diamagnetic materials continually increase or decrease,
608 respectively. Therefore, when exploring the remanence capability of complex natural samples that
609 are a mixture of magnetic carriers, it is necessary to correct the high-field portion for non-saturating
610 components. *HystLab* supports two standard approaches: a linear high-field slope correction, and
611 an approach to saturation correction (Fabian, 2006; Jackson and Solheid, 2010).

612 The linear correction assumes that the high-field portion of the ferromagnetic component is
613 saturated and fits a linear model to the high-field data to correct the slope by removing the
614 antiferro-, para- and diamagnetic contributions (i.e., non-saturated components). The approach to

615 saturation correction assumes that the high-field portion of the ferromagnetic component is not yet
616 fully saturated, but is in the reversible regime approaching saturation. This method fits the high-
617 field data with a model of the form:

$$618 \quad M(B) = \chi_{HF} B + M_s + \alpha B^\beta, \quad (5)$$

619 where χ_{HF} is the high-field susceptibility, M_s is the saturation moment, and α and β are approach to
620 saturation coefficients (Fabian, 2006; Jackson and Solheid, 2010). The approach to saturation
621 model is fitted similarly to the method outlined by Jackson and Solheid (2010), whereby 100 β
622 values evenly distributed on the interval [-2, -1] are specified and equation 5 is solved to determine
623 the remaining coefficients and the model that best fits the data.

624 *HystLab* includes an automated slope correction routine that tests if a high-field slope correction
625 should be applied and then tests the appropriateness of a linear correction versus an approach to
626 saturation correction at 70%, 80%, and 90% of the peak field. A schematic outline of the decision
627 process is shown in Figure 9.

628 The first step is to perform a lack-of-fit F-test for whole loop linearity using the data before slope
629 correction (Jackson and Solheid, 2010). This test assesses if the lack-of-fit between the data and a
630 linear model fit to the whole loop is significant. If the p-value of this test is < 0.05 (5% significance
631 level) then we can reject the null hypothesis that the misfit between the data and a linear loop is
632 due to random noise, hence conclude that it is primarily due to a lack-of-fit (i.e., the loop is not
633 linear). If the null hypothesis cannot be rejected (i.e., the whole loop appears linear) then no high-
634 field slope correction is applied.

635 If a linear loop is rejected, *HystLab* assesses whether the loop is closed at high-fields. Loops that
636 are distinctly open at high-fields indicate that a specimen is not saturated and not in the approach
637 to saturation regime (e.g., Figure 10a). In such cases, no form of high-field slope correction can
638 currently be applied.

639 Here we introduce two new statistics to assess loop closure at high-fields. First, at a given field
640 above which closure is to be tested, the signal-to-noise ratio (SNR) of the high-field M_{rh} curve to
641 high-field noise is assessed – An open loop will have a non-zero M_{rh} curve over the defined high-

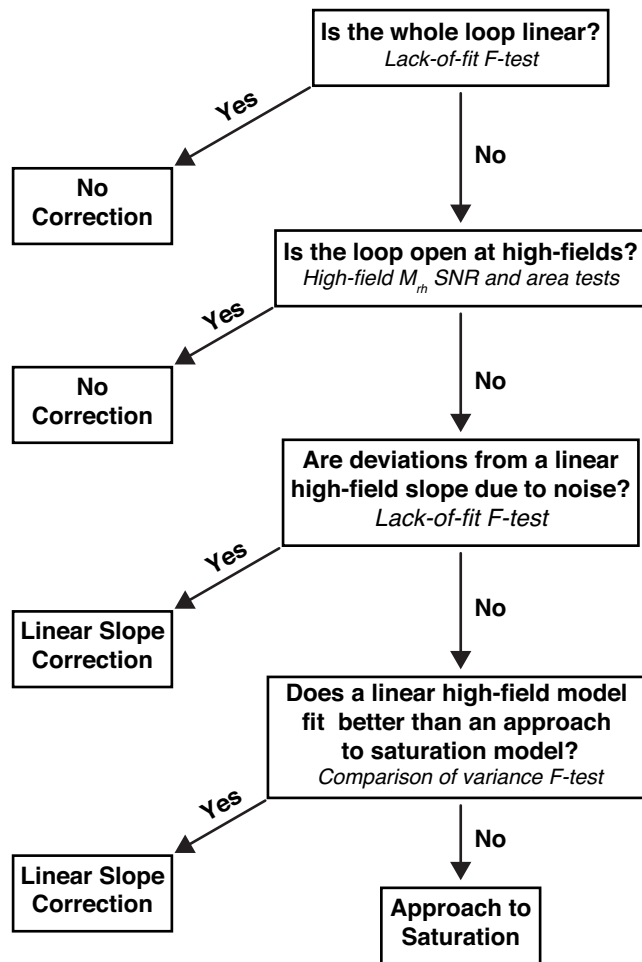
642 field range, which should be distinctive above the noise (i.e., have a high SNR). To assess the M_{rh}
643 signal, the negative field M_{rh} curve is inverted around the origin and averaged with the positive field
644 half and all negative moments are set to zero (they are a result of noise and setting them to zero
645 removes them from the estimation of signal power). The M_{rh} signal power is taken as the RMS of
646 this average M_{rh} curve. The power of the noise is taken as the RMS of the high-field noise and the
647 SNR is calculated in decibels as $20 \times \log_{10}(\text{signal}/\text{noise})$. High values of SNR indicate the non-zero
648 nature of the M_{rh} curve is distinct above the noise and indicate that the loop may be open.

649 The second statistic assesses the relative contribution of the high-field M_{rh} signal to the entire M_{rh}
650 signal. A perfectly closed loop will have zero area under the high-field portion of the M_{rh} curve, but
651 for most real data measurements the high-field M_{rh} is non-zero and a level tolerance is needed to
652 assess loop closure. To assess this, we define the high-field area ratio (HAR), which is the ratio of
653 the area under the high-field M_{rh} curve to the area under the entire M_{rh} curve. The areas are
654 calculated using the averaged M_{rh} curve described above and, following the SNR calculation, HAR
655 is calculated in dB. High values of HAR indicate that the high-field portion of the M_{rh} curve forms a
656 notable part of the total curve and indicate that the loop may be open; extremely low values
657 indicate that the high-field contribution is small and the loop may reasonably be assumed to be
658 closed.

659 The automatic correction determines that a loop is closed if the SNR is less than 8 dB or the HAR
660 is less than -48 dB. An 8 dB SNR corresponds to an average M_{rh} signal ~ 2.5 times stronger than
661 the noise, while an HAR of -48 dB corresponds to a high-field area $\sim 1/250^{\text{th}}$ of the total M_{rh} area.
662 These thresholds tend to prefer loop closure, for which high-field slope correction methods are
663 viable. For loops where closure is rejected, no correction is applied and the user should manually
664 consider the appropriateness of high-field slope corrections.

665 Figure 10a is an example of an open loop for which no correction can be rigorously applied. At
666 90% of the peak field, SNR = 15.8 dB and HAR = -47.8 dB. It is possible to test for closure at
667 higher peak fields, but it should be kept in mind that even minor loops that are far from saturation
668 will close at their peak field. Therefore, any loop will appear closed near the peak field.

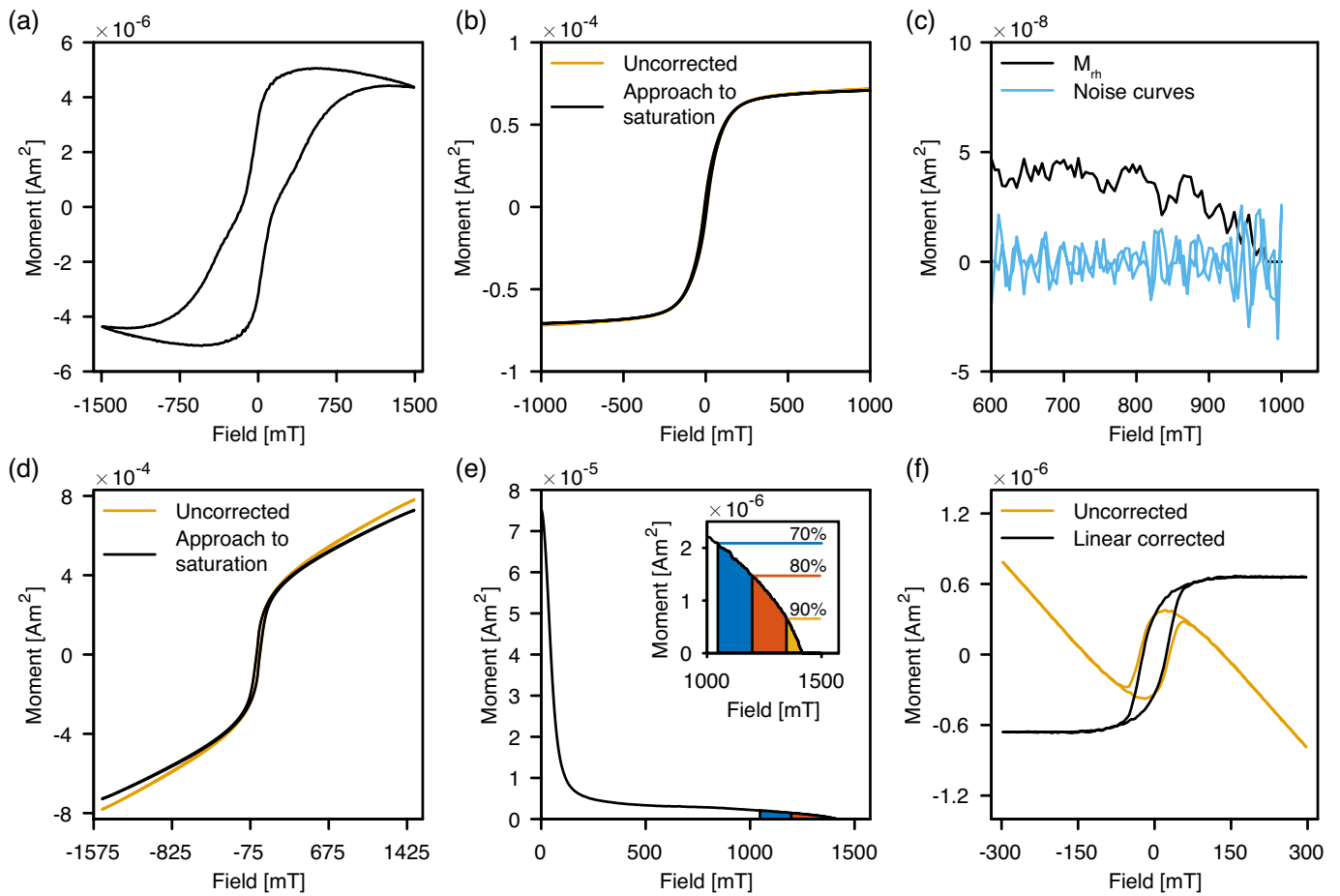
669



670

671 **Figure 9. Schematic of the decision process when applying an automated high-field slope**
 672 **correction.**

673



674

675 **Figure 10. Examples of high-field slope corrections.** (a) An oxidized granite specimen with
 676 mixed high and low coercivity components yields a hysteresis loop that remains open at high-
 677 fields. Currently, no high-field slope correction is strictly valid for such a loop. (b) A hysteresis loop
 678 of volcanic chip before and after automatic correction, which applies an approach to saturation
 679 correction. (c) The high-field averaged M_{rh} curve and high-field portions of the noise curve
 680 (negative field half inverted to positive fields) for the loop in part (b). At 70%, 80% and 90% of the
 681 peak field (700, 800 and 900 mT, respectively), M_{rh} signal-to-ratios are 10.6, 7.8, and 1.9 dB,
 682 respectively. (d) A hysteresis loop of a thermally stabilized basalt before and after automatic
 683 correction, which applies an approach to saturation correction. (e) The averaged M_{rh} curve for the
 684 loop in part (d), where the high-field portions used to calculate high-field to total M_{rh} signal ratios
 685 are shaded in color. The inset enlarges the high-field region. The HAR values at 70%, 80% and 90
 686 of the peak field are -24.7, -32.4, and -50.1 dB, respectively. Above 90% of the peak field, the loop
 687 can be considered closed. (f) An MTB specimen with a strong diamagnetic component. The
 688 automatic correction favors loop closure and a linear high-field slope correction.

689 In Figure 10b we show a hysteresis loop that visually appears to close at high-fields. The
690 corresponding high-field M_{rh} and noise curves are shown in Figure 10c. At 70%, 80% and 90% of
691 the peak field (700, 800 and 900 mT, respectively), M_{rh} SNR values are 10.6, 7.8, and 1.9 dB,
692 respectively. Above 80% of the peak field, the SNR falls just below our threshold of 8 dB and,
693 because M_{rh} becomes comparable to the level of noise, the loop can be considered closed. HAR at
694 the three field levels are -32.5, -38.0, and -49.4 dB.

695 In Figure 10d we show another loop that visually appears to be closed. In this case, the SNR
696 values at 70%, 80% and 90% of the peak field are all > 19.3 dB. The averaged M_{rh} curve is shown
697 in Figure 10e and the high-field areas are highlighted. The high-field regions have HAR values -
698 24.7, -32.4, -50.1 dB for 70%, 80%, and 90% of the peak field, respectively. These correspond to
699 total M_{rh} areas 17, 42, and 320 times larger than the respective high-field regions. The high SNR
700 values indicate the high-field M_{rh} segments are not unduly affected by noise, but the extremely low
701 HAR value at 90% peak field indicate the high-field M_{rh} signal is small and it is reasonable to
702 assume loop closure.

703 If an open loop is rejected, *HystLab* further tests the linearity of the high-field portion of the
704 hysteresis loop to evaluate whether a loop is saturated or approaching saturation (cf. Jackson and
705 Solheid, 2010). For a given field above which the specimen is assumed to be saturated or
706 approaching saturation, two styles of F-test are performed to assess which mode of slope
707 correction should be applied. Firstly, a linear model is fitted to the high-field data. Using the
708 negative high-field data as replicates of the positive high-field data, we perform a lack-of-fit F-test
709 to test the null hypothesis that the misfit between the data and the model can be explained by the
710 noise of the data. If the p-value of this test is < 0.05 (5% significance level), then we reject the null
711 hypothesis. That is, the poor fit of a linear model to the high-field data cannot be explained by
712 noise and may be better explained by an alternative model (i.e., approach to saturation).

713 The second test is an F-test comparison between the variance accounted for by a linear model
714 (with 2 free parameters) and the variance accounted for by an approach to saturation model (with
715 4 free parameters). If the p-value of this test is < 0.05 (5% significance level), then we reject the

716 null hypothesis that the simpler linear model fits the data adequately and conclude that the more
717 complex approach to saturation model is justified.

718 If one or both of these F-tests come out in favor of a linear high-field slope, a linear high-field
719 correction is applied. Only if both tests reject linearity is an approach to saturation correction
720 applied. This automated approach tends to favor applying a linear high-field slope correction
721 because of the ill-conditioned nature of the approach to saturation correction (see Jackson and
722 Solheid (2010) for a full discussion of the challenges of applying an approach to saturation
723 correction). We note that the F-tests are for general guidance and can be influenced by the
724 smoothing introduced by loop interpolation and drift corrections. For specimens where the
725 automated correction suggests approach to saturation, we recommend consideration of the
726 physical validity of the correction and a careful inspection and manual checking of fields around the
727 field above which the correction is applied. Furthermore, if possible, measuring hysteresis to higher
728 peak fields can help better resolve the saturation regime of many specimens.

729 The loops shown in Figure 10b and d are examples where a linear high-field slope is rejected and
730 an approach to saturation correction is applied. In Figure 10f we show a hysteresis loop from an
731 MTB specimen with a strong diamagnetic signal (the offset corrected loop shown in Figure 7a).
732 Both F-tests cannot reject a linear high-field slope, hence a linear correction is applied.

733 **4.6 Loop fitting**

734 During data processing, *HystLab* also fits the hysteresis loops following similar procedures to von
735 Dobeneck (1996) and Jackson and Solheid (2010). These fitted loops can be used to estimate the
736 hysteresis parameters from noisy data, but are not a substitute for re-measuring extremely noisy
737 data. How well the model fits the observed data is assessed by a lack-of-fit F-test (Jackson and
738 Solheid, 2010).

739 Firstly, the remanent (M_{rh}) and induced (M_{ih}) hysteretic curves are calculated (von Dobeneck,
740 1996). The negative field halves are inverted and averaged with the positive field halves to reduce
741 noise – *HystLab* fits to these averaged half curves. Like Jackson and Solheid (2010), *HystLab* fits
742 a combination of hyperbolic and sigmoid logistic basis functions to the M_{rh} and M_{ih} curves. In

743 *HystLab*, however, the basis functions are not a pre-defined set, but are defined for each specimen
744 such that the median fields of the basis functions correspond to equally spaced moments on the
745 M_{rh} and M_{ih} curves.

746 For each curve, a maximum of 22 basis functions are fitted, for a total maximum of 44 per
747 hysteresis loop. The M_{rh} curve is fitted with 10 hyperbolic secant functions, 10 sigmoid logistic
748 functions, and 2 linear functions with positive and negative slopes. The M_{ih} curve is fitted with 10
749 hyperbolic tangent functions, 10 sigmoid logistic functions, and 2 linear functions (to account for
750 any paramagnetic and diamagnetic components of uncorrected loops). The mathematical form of
751 the basis functions is given in the *HystLab* instruction manual (see also von Dobeneck, 1996;
752 Jackson and Solheid, 2010). Where insufficient data are available to perform the lack-of-fit F-test,
753 *HystLab* reduces the number of hyperbolic and sigmoid functions to less than 10 each.

754 The relative contribution of the basis functions is estimated using the sparse unmixing by variable
755 splitting and augmented Lagrangian (SUnSAL) algorithm of (Bioucas-Dias, 2009). In addition to the
756 sparsity enforced by SUnSAL, basis functions with a relative contribution of $< 0.01\%$ are omitted
757 from the final fit to minimize the total number of used functions.

758 The quality of the fit is assessed using the F-test for lack-of-fit (Jackson and Solheid, 2010). This
759 lack-of-fit test, which is performed on the whole hysteresis loop, tests the null hypothesis that the
760 misfit between the model and the data can be attributed to i.i.d. Gaussian noise. If the p-value of
761 this test is < 0.05 (5% significance level), then we can reject the null hypothesis. That is, the poor
762 fit of the basis functions to the loop cannot be explained by noise. In these cases, the quality of the
763 data should be sufficient to estimate the various hysteresis statistics from the data directly. Users
764 should consider each specimen carefully and note the F-test results are for guidance and can be
765 influenced by the smoothing introduced by loop interpolation and drift corrections.

766 In **Figure 11a**, we show an example of a visibly noisy loop and its fit (the loop is one of the 30
767 repeated loops measured in continuous mode with 100 ms averaging described in Section 3.1). In
768 **Figure 11b** we also show a higher quality, lower noise loop from the same specimen alongside the
769 fit to the loop in **Figure 11a** (the lower noise loop is the average of the 30 loops measured in
770 discrete field sweep mode with a pause time of 300 ms and 200 ms averaging time). The RMS

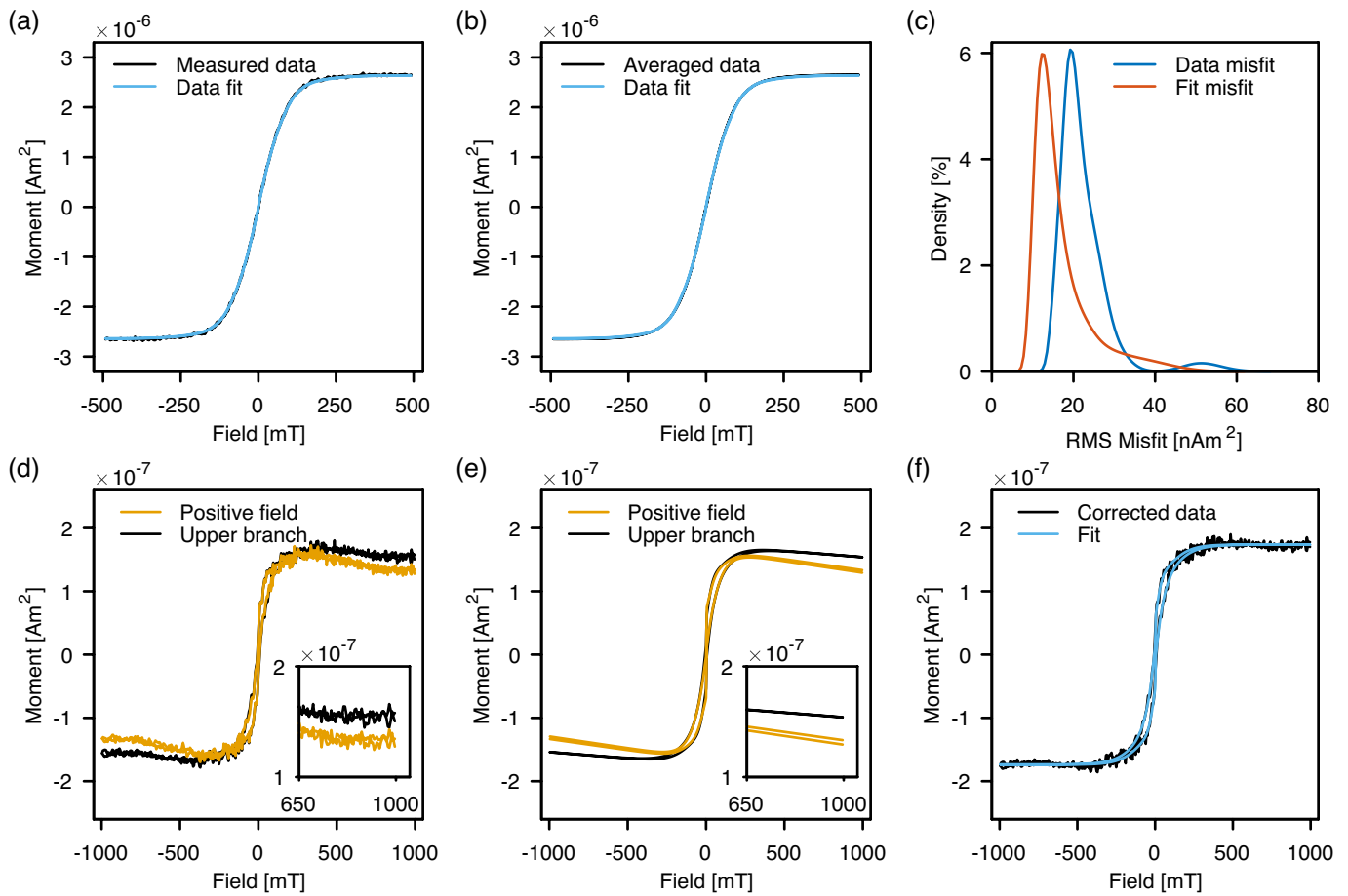
771 misfit between the measured loop and the averaged loop is $2.03 \times 10^{-8} \text{ Am}^2$ and the RMS misfit
772 between the loop fit and the averaged loop is $1.40 \times 10^{-8} \text{ Am}^2$, indicating that the fit to the lower
773 quality data is a better estimate of the higher quality loop. In **Figure 11c** we plot the density
774 distributions of the RMS misfits between higher quality averaged loop and (1) the 30 noisier loops
775 and (2) the model fits to the 30 noisier loops. For 24 of the 30 loops the model fit more accurately
776 represents the lower noise loop than the measured data, which illustrates how fitting hysteresis
777 loops can help to filter noisy data.

778 Fitting loops can also be a useful diagnostic tool for determining appropriate processing for noisy
779 or otherwise problematic loops. The hysteresis loops for a weak carbonate specimen (Jackson and
780 Swanson-Hysell, 2012) after positive field drift correction and after upper branch correction are
781 shown in **Figure 11d** (a linear high-field slope correction has been applied to both loops); the loop
782 closure errors are $7.03 \times 10^{-9} \text{ Am}^2$ and $7.60 \times 10^{-9} \text{ Am}^2$, respectively. Note the upward and downward
783 curvature in strong positive and negative fields, respectively. In the absence of a metamagnetic
784 transition, such curvature can be assumed to be the result of an unknown experimental artifact. A
785 comparison between the fits to these two loops is shown in **Figure 11e**. The fit to the positive field
786 drift corrected loop does not close (parallel and non-intersecting high-field upper and lower
787 branches; inset **Figure 11e**), but the fit to the upper branch corrected loop yields a more closed
788 loop, indicating it is a more appropriate drift correction to apply for this specimen.

789 In both cases, however, the high-field slope correction underestimates the high-field diamagnetic
790 susceptibility. As a consequence, after linear high-field slope corrections, both loops and their fits
791 have negative high-field slopes – the correction is inadequate. This incomplete correction is due to
792 unusual high-field drift, present in all four high-field segments, that results in slight anomalous
793 curvature of the high-field segments (**Figure 11d**). *HystLab* provides the option to apply slope
794 correction and estimate loop parameters for the fitted loop in addition to the measured data. The
795 resultant loop after upper branch drift correction using the fitted loop to correct the high-field slope
796 with a linear correction is shown in **Figure 11f**. Applying the slope correction to the fitted loop
797 yields more satisfactory high-field behavior that fully corrects for the diamagnetic component.

798 Fitting a noisy hysteresis loop can have a number of advantages, including removing high
799 frequency noise as well a means of assessing the appropriateness of processing and correcting
800 high-field slope behavior. We emphasize, however, that although fitting can help to analyze noisy
801 data, it is no substitute for remeasuring extremely noisy hysteresis loops.

802



803

804 **Figure 11. Examples of hysteresis loop fitting.** (a) Fitting of a loop measured with a 100 ms
 805 averaging time in continuous sweep mode. (b) The average of 30 loops for the same specimen in
 806 part (b), but measured with a 200 ms averaging time in discrete sweep mode with 200 ms settling
 807 time. The fitted loop is the same as shown in part (a). (c) The distribution of misfits between 30
 808 replicates of the loop shown in part (a) and the averaged loop in part (b) (blue curve) and the
 809 distribution of misfits between the model fits to the 30 repeat loops and the averaged loop in part
 810 (b) (orange curve). Twenty-four of the 30 replicates have model fits that more accurately represent
 811 the higher quality loop than the original measurements. (d) A weak carbonate specimen after
 812 positive field and upper branch drift corrections, both of which yield apparently similarly closed
 813 loops. The high-field region is expanded in the inset. (e) Fitting results of the loops shown in (d)
 814 reveal a distinct lack of loop closure after positive field drift correction. The high-field region is
 815 expanded in the inset. (f) Using the high-field segment of the fitted loop yields a better linear slope
 816 correction than using the data directly.

817

818 **5 *HystLab* features**

819 **5.1 *Supported data***

820 Within the rock and paleomagnetic community, a range of magnetometers can be used to measure
821 hysteresis loop data. These include vibrating sample magnetometers (VSMs), alternating gradient
822 magnetometers (AGMs), variable field translation balances (VFTBs), as well as superconducting
823 quantum interference device (SQUID) magnetometers coupled with high-field magnets. This
824 variety, combined with a range of manufacturers, means that numerous data formats are available,
825 which can complicate consistent analysis.

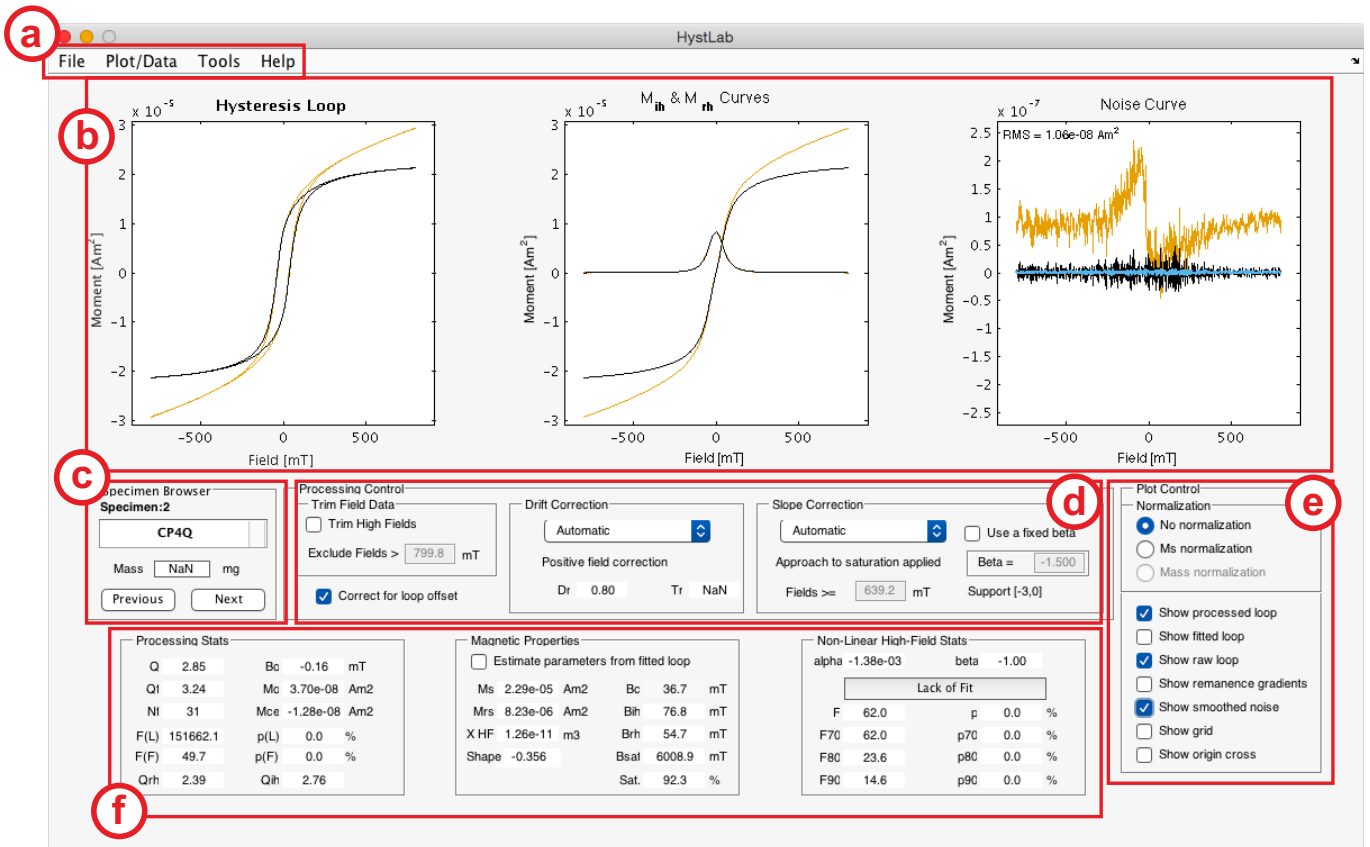
826 *HystLab* supports the most widely used data formats including, multiple format versions for the
827 Princeton Measurements Corporation MicroMag 3900 VSM and 2900 AGM, Lake Shore 7400 and
828 8600 VSMs, Quantum Designs Magnetic Properties Measurement System (MPMS), Magnetic
829 Measurements VFTBs, and MicroSense VSMs. *HystLab* allows users to append data to the
830 current session, which allows multiple data formats to be loaded and analyzed together. Once data
831 are loaded into *HystLab* users can save their *HystLab* session, allowing them to complete their
832 analyses at a later date or to share their results with collaborators. If any users encounter an
833 unsupported data format, they should contact the authors with an example file and it will be added
834 to *HystLab*.

835 **5.2 *Interface***

836 The main *HystLab* window is shown in Figure 12. Data can be loaded via the menu bar (Figure
837 12a) and will be plotted in the three main plots (Figure 12b). Here, the original, raw data can be
838 plotted alongside the processed data as well as the fitted data. In addition to the hysteresis loop,
839 the remanent (M_{rh}) and induced (M_{ih}) hysteretic curves, as well as the noise curve are also shown
840 (Figure 12b). Multiple specimens can be loaded at once and the user can browse through each
841 (Figure 12c). On loading data, loops are processed to correct for offset and apply the automatic
842 drift and high-field slope corrections. Additional processing can then be performed on a specimen-
843 by-specimen basis using the control panel shown in Figure 12d. The plot control panel (Figure
844 12e) allows for different moment/magnetization normalizations as well as controlling which data

845 are displayed. Panel f contains the analysis results and statistics – a comprehensive list and
 846 description of each statistic can be found the *HystLab* documentation (accessible through the
 847 “Help” menu, Figure 12a).

848



849

850 **Figure 12. The main *HystLab* interface.** (a) The menu bar for loading data and exporting results
 851 and plots. (b) The main field data plots. (c) Specimen browser. (d) The processing control panel. (e)
 852 The plot control panel. (f) The analysis results and statistics.

853

854 5.3 Data and plots

855 Statistics and analysis parameters in *HystLab* can be exported to tab delimited text files. The
 856 default plot color schemes are chosen to enhance contrast for colorblind users (Wong, 2011), but
 857 are fully customizable and can be saved to a user preference file for future use. In addition, by
 858 clicking on each plot, a new MATLAB figure window will open, which allows further customization.

859 All plots presented in *HystLab* can be exported to encapsulated postscript files that are publication
860 ready with little or no adjustment.

861 **6 Summary**

862 Magnetic hysteresis loops are one of the most ubiquitous rock magnetic measurements in the
863 Earth magnetism community. These rapid to measure data provide a diverse variety of descriptive
864 statistics that have a broad range of applications. However, despite their apparent ease and
865 simplicity, in-depth and quantitative descriptions of measuring and processing hysteresis loops to
866 avoid or correct for widely occurring detrimental factors (e.g., drift and loop offset) are rarely
867 performed.

868 Here we have outlined a range of approaches that can be used to improve the measurement
869 quality of hysteresis loops. Although these are largely developed from extensive experience using
870 VSM systems, many are applicable to a wide range of instruments used to measure magnetic
871 hysteresis. These strategies are also valid for other types of data measurable on the same
872 equipment (e.g., isothermal remanent magnetization acquisition, back-field demagnetization, first-
873 order reversal curves, among others).

874 Building on established processing recommendations, we have developed *HystLab*, which is a
875 new software package for the advanced processing and analysis of hysteresis loop data.
876 Supporting a wide range of data formats, with the ability to export data and generate publication
877 ready figures, *HystLab* has a range of tools to correct for commonly occurring negative artifacts in
878 hysteresis data. We hope that *HystLab* can enhance both productivity and accuracy when
879 processing and analyzing large data sets, and we encourage users with suggestions or bug
880 reports to contact us and help to improve the software.

881

882 **Appendix: Glossary of Hysteresis Statistics and Parameters**

883 Below is brief glossary of the major terms used in this paper. Further details and definitions are
884 given in the documentation that accompanies *HystLab*.

885	α	The alpha parameter for the applied approach to saturation high-field slope
886		correction (Fabian, 2006; Jackson and Solheid, 2010).
887	β	The beta parameter for the applied approach to saturation high-field slope correction
888		(Fabian, 2006; Jackson and Solheid, 2010).
889	B_0	Hysteresis loop offset along the field (horizontal) axis.
890	B_c	Hysteresis loop coercivity.
891	B_{ih}	The median value of the induced hysteretic curve (von Dobeneck, 1996).
892	B_{rh}	The median value of the remanent hysteretic curve (von Dobeneck, 1996).
893	HAR	The high-field area ratio (HAR). The ratio (in dB) of the area under the high-field M_{rh}
894		curve to the area under the entire M_{rh} curve.
895	M_0	Hysteresis loop offset along the moment/magnetization (vertical) axis.
896	M_{ce}	Hysteresis loop closure error (Jackson and Solheid, 2010). This is calculated as the
897		difference between the moment of the initial positive field and the moment in the
898		final positive field.
899	M_f	Ferromagnetic moment/magnetization at a specific field.
900	M_{ih}	The induced hysteric moment/magnetization curve (Rivas et al., 1981; von
901		Dobeneck, 1996). Calculated as half the sum of the upper and lower hysteresis
902		branches.
903	M_p	Paramagnetic moment/magnetization at a specific field.
904	M_{rh}	The remanent hysteric moment/magnetization curve (Rivas et al., 1981; von
905		Dobeneck, 1996). Calculated as half the difference of the upper and lower
906		hysteresis branches.
907	M_{rs}	Saturation remanent moment/magnetization.
908	M_s	Saturation moment/magnetization.

909	Q	A measure of the quality of the raw hysteresis loop determined by taking the linear
910		correlation between the upper and inverted lower branches.
911	Q_f	A measure of the quality of the slope-corrected (ferromagnetic) hysteresis loop
912		determined by taking the linear correlation between the upper and inverted lower
913		branches.
914	Q_{ih}	A measure of the quality of the processed M_{ih} curve determined by taking the linear
915		correlation between the positive field half and the inverted negative field half.
916	Q_{rh}	A measure of the quality of the processed M_{rh} curve determined by taking the linear
917		correlation between the positive field half and the reflected negative field half.
918	<i>Shape</i>	Hysteresis loop shape factor, σ (Fabian, 2003).
919	<i>SNR</i>	The signal-to-noise ratio (SNR; in dB) of the high-field M_{rh} to the high-field noise.
920	T_0	The initial temperature of a specimen at the beginning of a measurement.
921	T_A	The ambient temperature between the pole pieces of the measurement equipment.
922	T_r	The ratio of the specimen initial temperature (T_0) to the ambient temperature
923		between the pole pieces (T_A). Estimated for the paramagnetic drift correction.
924	X_{HF}	High-field susceptibility (determined from the high-field slope correction).

925

926 ***Acknowledgements***

927 We thank Andy Biggin, Liao Chang, Cao Changqian, Mimi Hill, Jinhua Li, Suzhen Liu, Adrian
928 Muxworthy, Eduard Petrovsky, Daniele Thallner, Yuhji Yamamoto, and Lake Shore Cryotronics for
929 providing test data. Richard Bono and Peat Solheid are thanked for their thoughts and discussion.
930 We are very grateful to Harry Reichard and Brad Dodrill of Lake Shore Cryotronics for their
931 valuable discussion on this work and their help and advice over many years. GAP acknowledges
932 funding from a NERC Independent Research Fellowship (NE/P017266/1) and NSFC grants
933 41574063 and 41621004, and CAS project XDB18010203. MJ acknowledges support of the

934 Institute for Rock Magnetism, funded by the NSF Instruments and Facilities program and by the
935 University of Minnesota.

936

937 **References**

- 938 Bioucas-Dias, J.M., 2009. A variable splitting augmented Lagrangian approach to linear spectral
939 unmixing. In: First IEEE GRSS workshop on Hyperspectral Image and Signal Processing:
940 WHISPERS 2009, 1-4, doi: 10.1109/WHISPERS.2009.5289072.
- 941 Carvalho, C., Roberts, A.P., Leonhardt, R., Laj, C., Kissel, C., Perrin, M., Camps, P., 2006.
942 Increasing the efficiency of paleointensity analyses by selection of samples using first-order
943 reversal curve diagrams. *J. Geophys. Res.*, 111, B12103, doi: 10.1029/2005JB004126.
- 944 Chang, L., Bolton, C.T., Dekkers, M.J., Hayashida, A., Heslop, D., Krijgsman, W., Kodama, K.,
945 Paterson, G.A., Roberts, A.P., Rohling, E.J., Yamamoto, Y., Zhao, X., 2016. Asian
946 monsoon modulation of nonsteady state diagenesis in hemipelagic marine sediments
947 offshore of Japan. *Geochem. Geophys. Geosyst.*, 17, 4383-4398, doi:
948 10.1002/2016GC006344.
- 949 Chen, A., Egli, R., Moskowitz, B.M., 2005. A FORC in the Road? *IRM Quarterly*, 15, 8-11.
- 950 Dodrill, B.C., n. d. The Performance of the Model 7400 VSM: Sensitivity,
951 ([http://www.lakeshore.com/Documents/The_Performance_of_the_Model_7400_VSM](http://www.lakeshore.com/Documents/The_Performance_of_the_Model_7400_VSM_Sensitivity.pdf)
952 [Sensitivity.pdf](http://www.lakeshore.com/Documents/The_Performance_of_the_Model_7400_VSM_Sensitivity.pdf)), accessed Nov. 2017.
- 953 Fabian, K., 2003. Some additional parameters to estimate domain state from isothermal
954 magnetization measurements. *Earth Planet. Sci. Lett.*, 213, 337-345, doi: 10.1016/S0012-
955 821X(03)00329-7.
- 956 Fabian, K., 2006. Approach to saturation analysis of hysteresis measurements in rock magnetism
957 and evidence for stress dominated magnetic anisotropy in young mid-ocean ridge basalt.
958 *Phys. Earth Planet. Inter.*, 154, 299-307, doi: 10.1016/j.pepi.2005.06.016.
- 959 Haag, M., Dunn, J.R., Fuller, M.D., 1995. A new quality check for absolute palaeointensities of the
960 Earth magnetic field. *Geophys. Res. Lett.*, 22, 3549-3552, doi: 10.1029/95GL03333.
- 961 Harrison, R.J., McEnroe, S.A., Robinson, P., Carter-Stiglitz, B., Palin, E.J., Kasama, T., 2007. Low-
962 temperature exchange coupling between Fe₂O₃ and FeTiO₃: Insight into the mechanism
963 of giant exchange bias in a natural nanoscale intergrowth. *Phys. Rev. B*, 76, 174436.
- 964 Hatfield, R.G., Stoner, J.S., Reilly, B.T., Tepley, F.J., Wheeler, B.H., Housen, B.A., 2017. Grain
965 size dependent magnetic discrimination of Iceland and South Greenland terrestrial
966 sediments in the northern North Atlantic sediment record. *Earth Planet. Sci. Lett.*, 474, 474-
967 489, doi: 10.1016/j.epsl.2017.06.042.
- 968 Housen, B.A., Banerjee, S.K., Moskowitz, B.M., 1996. Low-temperature magnetic properties of
969 siderite and magnetite in marine sediments. *Geophys. Res. Lett.*, 23, 2843-2846, doi:
970 10.1029/96GL01197.
- 971 Jackson, M., Solheid, P., 2010. On the quantitative analysis and evaluation of magnetic hysteresis
972 data. *Geochem. Geophys. Geosyst.*, 11, Q04Z15, doi: 10.1029/2009GC002932.
- 973 Jackson, M., Swanson-Hysell, N.L., 2012. Rock magnetism of remagnetized carbonate rocks:
974 another look, in: *Geol. Soc. London Spec. Pub*, vol. 371, edited by, pp. 229-251, doi:
975 10.1144/sp371.3.
- 976 Kissel, C., Guillou, H., Laj, C., Carracedo, J.C., Nomade, S., Perez-Torrado, F., Wandres, C.,
977 2011. The Mono Lake excursion recorded in phonolitic lavas from Tenerife (Canary
978 Islands): Paleomagnetic analyses and coupled K/Ar and Ar/Ar dating. *Phys. Earth Planet.*
979 *Inter.*, 187, 232-244, doi: 10.1016/j.pepi.2011.04.014.
- 980 Krása, D., Wilkinson, C.D.W., Gadegaard, N., Kong, X., Zhou, H., Roberts, A.P., Muxworthy, A.R.,
981 Williams, W., 2009. Nanofabrication of two-dimensional arrays of magnetite particles for
982 fundamental rock magnetic studies. *J. Geophys. Res.*, 114, B02104, doi:
983 10.1029/2008JB006017.

- 984 Lagarias, J., Reeds, J., Wright, M., Wright, P., 1998. Convergence properties of the Nelder-Mead
 985 simplex method in low dimensions. *SIAM J. Optimiz.*, 9, 112-147, doi:
 986 10.1137/S1052623496303470.
- 987 Li, J., Pan, Y., Liu, Q., Yu-Zhang, K., Menguy, N., Che, R., Qin, H., Lin, W., Wu, W., Petersen, N.,
 988 Yang, X.a., 2010. Biomineralization, crystallography and magnetic properties of bullet-
 989 shaped magnetite magnetosomes in giant rod magnetotactic bacteria. *Earth Planet. Sci.*
 990 *Lett.*, 293, 368-376, doi: 10.1016/j.epsl.2010.03.007.
- 991 Li, J., Wu, W., Liu, Q., Pan, Y., 2012. Magnetic anisotropy, magnetostatic interactions and
 992 identification of magnetofossils. *Geochem. Geophys. Geosyst.*, 13, Q10Z51, doi:
 993 10.1029/2012GC004384.
- 994 Li, S., Yang, Z., Deng, C., He, H., Qin, H., Sun, L., Yuan, J., van Hinsbergen, D.J.J., Krijgsman,
 995 W., Dekkers, M.J., Pan, Y., Zhu, R., 2017. Clockwise rotations recorded in redbeds from
 996 the Jinggu Basin of northwestern Indochina. *Geol. Soc. Am. Bull.*, doi: 10.1130/b31637.1.
- 997 Lin, W., Pan, Y., 2009. Uncultivated Magnetotactic Cocci from Yuandadu Park in Beijing, China.
 998 *Applied and Environmental Microbiology*, 75, 4046-4052, doi: 10.1128/aem.00247-09.
- 999 Liu, S., Deng, C., Xiao, J., Li, J., Paterson, G.A., Chang, L., Yi, L., Qin, H., Pan, Y., Zhu, R., 2015.
 000 Insolation driven biomagnetic response to the Holocene Warm Period in semi-arid East
 001 Asia. *Sci. Rep.*, 5, 8001, doi: 10.1038/srep08001.
- 002 Liu, S., Deng, C., Xiao, J., Li, J., Paterson, G.A., Chang, L., Yi, L., Qin, H., Zhu, R., 2016. High-
 003 resolution enviromagnetic records of the last deglaciation from Dali Lake, Inner Mongolia.
 004 *Palaeogeogr. Palaeoclimatol. Palaeoecol.*, 454, 1-11, doi: 10.1016/j.palaeo.2016.04.030.
- 005 Muxworthy, A.R., Bland, P.A., Davison, T.M., Moore, J., Collins, G.S., Ciesla, F.J., 2017. Evidence
 006 for an impact-induced magnetic fabric in Allende, and exogenous alternatives to the core
 007 dynamo theory for Allende magnetization. *Meteorit. Planet. Sci.*, 2132-2146, doi:
 008 10.1111/maps.12918.
- 009 Muxworthy, A.R., Heslop, D., Paterson, G.A., Michalk, D., 2011. A Preisach method for estimating
 010 absolute paleofield intensity under the constraint of using only isothermal measurements: 2.
 011 Experimental testing. *J. Geophys. Res.*, 116, B04103, doi: 10.1029/2010jb007844.
- 012 Muxworthy, A.R., Matzka, J., Petersen, N., 2001. Comparison of magnetic parameters of urban
 013 atmospheric particulate matter with pollution and meteorological data. *Atmospheric*
 014 *Environ.*, 35, 4379-4386, doi: 10.1016/S1352-2310(01)00250-3.
- 015 Pan, Y., Petersen, N., Davila, A.F., Zhang, L., Winklhofer, M., Liu, Q., Hanzlik, M., Zhu, R., 2005.
 016 The detection of bacterial magnetite in recent sediments of Lake Chiemsee (southern
 017 Germany). *Earth Planet. Sci. Lett.*, 232, 109-123, doi: 10.1016/j.epsl.2005.01.006.
- 018 Paterson, G.A., Heslop, D., Pan, Y., 2016. The pseudo-Thellier palaeointensity method: new
 019 calibration and uncertainty estimates. *Geophys. J. Int.*, 207, 1596-1608, doi:
 020 10.1093/gji/ggw349.
- 021 Paterson, G.A., Muxworthy, A.R., Roberts, A.P., Mac Niocaill, C., 2010. Assessment of the
 022 usefulness of lithic clasts from pyroclastic deposits for paleointensity determination. *J.*
 023 *Geophys. Res.*, 115, B03104, doi: 10.1029/2009JB006475.
- 024 Paterson, G.A., Muxworthy, A.R., Yamamoto, Y., Pan, Y., 2017. Bulk magnetic domain stability
 025 controls paleointensity fidelity. *Proc. Natl. Acad. Sci. U.S.A.*, 114, 13120-13125, doi:
 026 10.1073/pnas.1714047114.
- 027 Paterson, G.A., Wang, Y., Pan, Y., 2013. The fidelity of paleomagnetic records carried by
 028 magnetosome chains. *Earth Planet. Sci. Lett.*, 383, 82-91, doi: 10.1016/j.epsl.2013.09.031.
- 029 Rivas, J., Zamarro, J., Martin, E., Pereira, C., 1981. Simple approximation for magnetization
 030 curves and hysteresis loops. *IEEE Trans. Magn.*, 17, 1498-1502, doi:
 031 10.1109/TMAG.1981.1061241.
- 032 Tikoo, S.M., Weiss, B.P., Shuster, D.L., Suavet, C., Wang, H., Grove, T.L., 2017. A two-billion-year
 033 history for the lunar dynamo. *Sci. Adv.*, 3, doi: 10.1126/sciadv.1700207.
- 034 Van Hinsbergen, D.J.J., Straathof, G.B., Kuiper, K.F., Cunningham, W.D., Wijbrans, J., 2008. No
 035 vertical axis rotations during Neogene transpressional orogeny in the NE Gobi Altai:
 036 coinciding Mongolian and Eurasian early Cretaceous apparent polar wander paths.
 037 *Geophys. J. Int.*, 173, 105-126, doi: 10.1111/j.1365-246X.2007.03712.x.
- 038 von Dobeneck, T., 1996. A systematic analysis of natural magnetic mineral assemblages based on
 039 modelling hysteresis loops with coercivity-related hyperbolic basis functions. *Geophys. J.*
 040 *Int.*, 124, 675-694, doi: 10.1111/j.1365-246X.1996.tb05632.x.

041 Williams, W., Evans, M.E., Krása, D., 2010. Micromagnetics of paleomagnetically significant
042 mineral grains with complex morphology. *Geochem. Geophys. Geosyst.*, 11, Q02Z14, doi:
043 10.1029/2009GC002828.
044 Wong, B., 2011. Color blindness. *Nat. Methods*, 8, 441-441, doi: 10.1038/nmeth.1618.
045 Zhang, C., Appel, E., Qiao, Q., 2013. Heavy metal pollution in farmland irrigated with river water
046 near a steel plant—magnetic and geochemical signature. *Geophys. J. Int.*, 192, 963-974,
047 doi: 10.1093/gji/ggs079.
048 Zhang, R., Necula, C., Heslop, D., Nie, J., 2016. Unmixing hysteresis loops of the late Miocene–
049 early Pleistocene loess-red clay sequence. *Sci. Rep.*, 6, 29515, doi: 10.1038/srep29515.
050